2015

The Role of Mantle Residuum in Subduction-Driven Circulation: Implications for the Cascades System

Sara A. Szwaja
University of Rhode Island, sszwaja@gmail.com

THE ROLE OF MANTLE RESIDUUM IN SUBDUCTION-DRIVEN CIRCULATION: IMPLICATIONS FOR THE CASCADES SYSTEM

BY

SARA A SZWAJA

A THESIS SUBMITTED IN PARTIAL FULFILLMENT OF THE

REQUIREMENTS FOR THE DEGREE OF

MASTERS OF SCIENCE

IN

OCEANOGRAPHY

UNIVERSITY OF RHODE ISLAND

2015

MASTER OF SCIENCE THESIS

OF

SARA A SZWAJA

APPROVED:

Thesis Committee:

Major Professor Christopher Kincaid

Katherine Kelley

Dawn Cardace

Nasser H. Zawia
DEAN OF THE GRADUATE SCHOOL

UNIVERSITY OF RHODE ISLAND
2015

ABSTRACT

This paper investigates the role of upper mantle heterogeneity on circulation. We utilize a kinematic laboratory subduction model that drives multiple styles of three-dimensional, time dependent mantle circulation that interacts with residuum left behind after a major melt production and extraction event. Models of mantle-residuum interaction highlight the impact of melt-induced mantle chemical heterogeneity can have on return flow in convergent margins. Wedge chemical heterogeneity and subsequent melting influence mass and energy transport to the Earth's surface. These models are designed to represent aspects of the Cascadia subduction zone of the Pacific Northwest U.S., a geologically challenging area where the ~20 Ma Columbia River/Steens flood basalt (CSFB) event transitions to the age-progressive volcanic tracks along the High Lava Plains (HLP) and Snake River Plain-Yellowstone (SRP). This region is a focal point for debate over the applicability of mantle plume models. A series of lab models have tested plume or non-plume explanations for the Cascades-Yellowstone volcanism. We report on non-plume results that indicate that a non-plume explanation, in which trench-normal volcanic tracks form naturally from deformation of residuum from a CSFB-type event. Melt generating patterns show that our models readily explain bimodal melting beneath the HLP and SRP regions and the westward progression of melt beneath the HLP. However, replicating the age-progressive melting patterns under the SRP remains a challenge for these experiments.

ACKNOWLEDGMENTS

I would like to express my sincere gratitude to my advisor, Dr. Christopher Kincaid. Four years ago I arrived at the Graduate School of Oceanography with a background in applied mathematics and finance. Chris showed infinite encouragement and patience as I learned the basics of geological and geophysical sciences. Without the many hours Chris dedicated to the lab, research discussion, and teaching I would not be leaving GSO as the confident, independent scientist that I am today. Infinite thanks, Chris!

This thesis benefited from helpful discussions with Kelsey Druken, Katie Kelley, and Dawn Cardace. I owe Julia MacDougall many thanks for spending numerous summer mornings conducting experiments with me in the Geophysical Fluid Dynamics Laboratory at GSO. A special thank you to my fiancé, Neal, for his unconditional love and encouragement. And as always, I am grateful for the support and love of my family and friends through all my life's adventures.

PREFACE

This thesis was written in manuscript form to be submitted as partial fulfillment for a Master of Science degree in Oceanography, at the University of Rhode Island. Funding for this study was provided by the National Science Foundation. I will be submitting this manuscript to Geochemistry, Geophysics, Geosystems (G-Cubed) for publication.

TABLE OF CONTENTS

ABSTRACT ii

ACKNOWLEDGMENTS iii

PREFACE iv

TABLE OF CONTENTS v

LIST OF TABLES vii

LIST OF FIGURES viii

MANUSCRIPT 1

1. Introduction 2

2. Overview: Post-20 Ma Pacific Northwest Volcanism 5

2.1 Geological Constraints 5

2.2 Melting Models 8

3. Laboratory Methods 11

3.1 Apparatus 11

3.2 Scaling 14

3.3 Experimental Method 15

3.4 Data Collection 20

4. Experimental Results 21

4.1 Time Evolution of Residuum: Rollback Subduction 22

4.1.1 Effect of an Overriding Plate 27

4.1.2 Effect of Back-Arc Extension 33

4.1.3 Effect of Residuum Initial Position 40

5. Discussion 41

6. Conclusions 48

References 50

SUPPLEMENTAL INFORMATION 76

LIST OF TABLES

TABLE PAGE

Table 1. Experimental parameters for plate forcing and residuum 57

Table 2. Comparison of constraints with models 58

LIST OF FIGURES

FIGURE PAGE

FIGURE 1. Geologic map of the Pacific-Northwest U.S. showing the Cascades subduction system with key volcanic features: Large igneous province Columbia River/Steens flood basalts (CSFB), shown in green, and southern volcanic tracks High Lava Plains (HLP) and Snake River Plain (SRP) are marked in pink and blue, respectively, and show opposite age progression of rhyolitic lavas in millions of years 59

FIGURE 2. (a) Photograph of the subduction apparatus with the tank of glucose syrup and the reinforced belt system representing subducting plate. White arrows indicate down-dip (U_D) and translational (U_T) slab motions controlled by piston motors located above fluid surface. (b) Scaled map-view cartoon of the lab apparatus. (c) Enlarged inset showing approximate center location of residuum at experiment initiation (yellow stars). In most cases, residuum location is on the slab centerline (star A). In the Cascadia cases (Table 1), residuum initial location is north of the slab centerline (star B) 60

FIGURE 3. Cartoon schematics illustrating model overriding plates and surface conditions. (a) OP and subducting slab migrate with trench motion. (b) The back-arc extension (BAE) axis moves with trench motion. Mylar spools out from the roller at ($-U_T$). Arrows indicate absolute motion of slab, trench, and extension axis. The OP has zero horizontal velocity and imposes a no slip surface condition on the mantle. The AP have free slip mantle surface 61

FIGURE 4. Comparison of map view, 20 Ma evolution of weak (a – c) and strong (d – f) residuum in subduction driven flows with U_T = 3 cm/min and U_D = 8 cm/min. Images show results at depth z = 1 – 2 cm (~ 65 – 130 km) beneath a free slip mantle surface. Residuum structure is highlighted in yellow. Downdip subduction entrains residuum material towards the trench while U_T-induced toroidal flow compresses the residuum towards the slab centerline. $\mu^* < 1$ experiences very efficient pure shear in transition from an initial north-south morphology to an east-west morphology. $\mu^* > 1$ resists internal deformation and folds along the trench-normal symmetry line..... 62

FIGURE 5. Late stage map view images of (a) – (b) weak residuum (Exp. 6) and (c) – (d) strong residuum (Exp. 5). Top row shows residuum-wedge after 60 My (7.5 minutes in the lab) and bottom row shows wedge results after 80 My (10 minutes in the lab)..... 63

FIGURE 6. (a) Wedge region divided into three analysis zones: Northern edge (black), mid-region (blue), and slab centerline (red). Grey dashes indicate averaging domains. (b) Average normalized flow direction (Φ^*) and (c – e) average instantaneous flow velocity (U_M/U_D) for case with weak (circles) and strong (squares) residuum. Velocities and direction are averaged from instantaneous flows in t^* = 0, 0.5, and 1. Grey shading indicates standard deviation in each averaging domain. $\delta U_M/U_D$ represents change in region average velocity between averaging domains located farthest and nearest to the trench 64

FIGURE 7. Lagrangian particle velocity for ambient wedge with (a) free slip and (b) no slip surface conditions. Results are in the x-y plane at z = 1 – 2 cm (65 –

130 km). All velocities are calculated in a fixed trench reference frame 65

FIGURE 8. (a) and (b) Identical to Fig. 7, except results are in the x-z plane, along the slab centerline from mantle surface to depth. (c) Average surface flow velocity vs. mantle depth from the shallow mantle domain shown in grey box from (a) and (b) 66

FIGURE 9. (a) Cartoon illustrating calculation of L^*. Experiment initial residuum length (L_0) is ~20 cm (1300 km). (b) Residuum north-south nondimensionalized length (L^*) over time. Except for Exp. 1a, where $U_T = 0$, all experiments are run with slab rates $U_T = 3$ cm min^{-1}, $U_D = 8$ cm min^{-1}. Toroidal flow induced by a migrating trench (U_T) is the major driver of deformation of the mantle wedge heterogeneity. In cases with OP, mantle material couples to the OP and resists toroidal flow deformation on the timescales of our experiments. *HLP/SRP N-S extent* red box represents the ~100 – 200 km trench-parallel (north-south) length of the HLP/SRP tracks estimated by seismic studies [e.g., *Wagner et al.*, 2012], and we've assumed a ± 50 km and ± 5 Ma error 67

FIGURE 10. Comparison of 20 Ma evolution of weak and strong residuum with free slip mantle surface (a – b) and with overriding plate (c – d). Dashed lines indicate mantle-residuum interface through time. With no OP (Exp. 13 and 14), greater residuum sinking velocities (up to 0.5 cm min^{-1}) are observed in $\mu^* > 1$. With coupled mantle surface (Exp. 12 and 15), upwelling velocities are detected beneath and on the west of the residuum. 68

FIGURE 11. Shallow wedge residuum volume vs. time. Residuum volume is

approximated assuming shallow mantle extends to 3 cm (~200 km) depth. Volume = side view area × residuum N-S extent (from x-y plane). Material subducted below 3 cm is considered flushed from shallow mantle. Imposing different mantle surface conditions, such as (a) free slip mantle (Exp. 13 & 14) and (b) no slip (Exp. 12 & 15), greatly changes patterns of material transport towards the trench and flushing from the shallow mantle 69

FIGURE 12. Low viscosity (a – c) and high viscosity (d – f) residuum beneath BAE axis with westward migration rate 3 cm min^{-1}. Rollback controlled BAE begins at $t^* = 0$. Extensional axis (green dashed line) is located ~13.5 cm (~900 km) from the trench. Residuum east of extension center is left behind as slab migrates to the west. (c) Weak heterogeneity splits into two at the extension axis. (d – f) Experiment illustrates strong stress guide effect. Viscous normal stresses limit slab-ward advection of residuum under AP. Approach velocity of western side of residuum ~1 cm min^{-1} is ~ two-thirds less than the weak heterogeneity case. After 20 Ma, this feature has remained robust throughout. 70

FIGURE 13. Normalized flow direction (Φ^*) and mean instantaneous wedge velocity (U_M/U_D) for BAE cases Exp. 27 (weak residuum) and Exp. 18 (strong residuum). The majority of the residuum mass is located in the slab centerline region and velocities in this region exhibit the greatest variation between weak and strong residuum cases..... 71

FIGURE 14. Side view evolution of (a) weak (Exp. 27) and (b) strong (Exp. 18) residuum located beneath a BAE axis. Dashed lines indicate residuum-wedge

interface through time. For reference, approximate locations of Cascades volcanic centers Newberry (N.), McDermitt (McD.), and Yellowstone (Y.) are shown in black triangles. (c) Mean Lagrangian upwelling velocity of particles located in shallow mantle (grey box in (a) and (b)) between $t^* = 0$ and 1. Grey shading represents standard deviation about the mean 72

FIGURE 15. (a) Anhydrous P-T diagram for mantle lherzolite (red curve, from *Thompson and Gibson* [2000]), and mantle harzburgite (purple curve, from *Maaløe* [2004]). Black lines represent the adiabats for representative mantle potential temperatures (T_P). Right-hand side y-axis shows mantle depths at which decompression melting expected for lherzolite, the assumed mantle composition, and harzburgite, the assumed residuum composition. (b) Potential trajectory and timing for a low viscosity residuum interface migration beneath the HLP. Residuum evolution due to slab and BAE induced upper mantle flow fields. Trenchward shallowing of sloped residuum interface leads to westward age progressive melting beneath the HLP. Residuum evolution is a guide for melting background ambient mantle 73

FIGURE 16. Time evolution of weak (a – c) and strong (d – f) residuum initially located in northern wedge beneath BAE axis with extension rate of 3 cm min^{-1}. In the $t^* = 0.5$ and $t^* = 1$ images, the initial residuum location is outlined in green for reference. Southward migration of residuum is the result of deformations induced by trench rollback 74

FIGURE 17. Annotations highlight rough estimates of key features of PNW overlaid on experiments with BAE and (a) weak (Exp. 30) and (b) strong (Exp. 23)

residuum. Laboratory models represent North-south offset between the CSFB and HLP-SRP tracks are a consequence of deformations induced by trench-migration. Our experiments indicate that placement of melt residuum beneath HLP and SRP is consequence of slab and OP plate forcing allowing E-W extension of features. 75

Manuscript

The role of mantle residuum in subduction-driven circulation:

Implications for the Cascades system

by

Sara A Szwaja, Christopher Kincaid*

Graduate School of Oceanography, University of Rhode Island
Narragansett, Rhode Island

Julia G. MacDougall

Department of Geological Sciences, Brown University
Providence, Rhode Island

In preparation for submission to Geochemistry, Geophysics, Geosystems (G-Cubed)

*Corresponding author:
Christopher Kincaid
Graduate School of Oceanography
University of Rhode Island
215 South Ferry Road
Narragansett, RI, 02882, USA
Phone: +1-401-874-6571
Email: kincaid@uri.edu

1. Introduction

Melting models tend to focus on the spatial and temporal patterns of surface volcanism, while less attention is paid to the residue of melting that continues to evolve in the mantle. The concept of mantle residuum has a long history in the geosciences literature, particularly in terms of continental tectosphere, where extraction of volatiles in partial melt creates a local separation between geotherm and solidus, driving up residuum viscosity (and buoyancy) relative to ambient mantle [*Jordan*, 1975, 1978; *Pollack*, 1986; *James et al.*, 2001]. While there have been some attempts to model time-varying evolution of mantle residuum in plate-driven flow fields [e.g., *Humphreys et al.*, 2000; *Smith et al.*, 2009], the phenomenon remains poorly understood. Our goal is to characterize the general aspects of flow-residuum interactions in subduction settings, with specific focus on the Cascades subduction system in the Pacific Northwest U.S.

The Cascadia subduction zone is a particularly complicated tectonomagmatic region. Most notable geologic events of the Cascades include the ~20 Ma creation of the large igneous province Columbia River/Steen flood basalts (CSFB) and subsequent (~12 Ma to present day) opposite age-progressive rhyolite tracks: Snake River Plain (SRP) and High Lava Plains (HLP) [*Geist and Richards*, 1993; *Camp and Ross*, 2004] (Fig. 1). Sinking of oceanic lithosphere with rollback and a mode of plate steepening, back-arc extension, lithospheric basal topography, and a mantle plume have each been implicated in the development of Northwestern U.S. volcanic patterns over the past 20 Ma [e.g., *Cross and Pilger*, 1978; *Christiansen et al.*, 2002; *Camp*

and Ross, 2004; *Jordan et al.*, 2004; *Hooper et al.*, 2007; *Long et al.*, 2012; *Kincaid et al.*, 2013]. One explanation for the time-progressive HLP/SRP volcanism invokes a CSFB residuum interacting with upper mantle circulation to account for the surface magmatic trends [e.g., *Humphreys et al.*, 2000; *Smith et al.*, 2009]. We employ kinematic 3D subduction modeling to test the hypothesis that the mantle heterogeneity left behind after the CSFB melting event can control the timing and location of volcanic activity on the surface. A goal is to test if plate-driven upper mantle flow interacting with an evolving shallow mantle residuum can create the bimodal, age-progressive volcanism beneath the HLP and SRP.

Laboratory models are employed to represent the deformation and entrainment of chemical heterogeneity, or residuum, present in the wedge due to a large melting event. Primary experiment variables include residuum viscosity and initial location, along with plate parameters such as subduction, trench migration, lithosphere-mantle coupling, and back-arc extension. In all cases of rollback subduction, the flow field influences the heterogeneity. Slab entrainment transports heterogeneities towards the trench while 3D return flow around the slab edge into the wedge controls residuum trench-parallel deformation and transportation. Extension in the overriding plate strongly controls residuum evolution and has important implications for the Cascades subduction system. Presence of weak or strong residuum produces distinct patterns in vertical flow, which should in turn influence spatial-temporal patterns in melt production. Upwelling related decompression melting driven by residuum-flow field interaction provides a source of melt beneath the HLP/SRP-Yellowstone regions.

However, the timing of that volcanism in our simplified model is not easily matched to the age-progressive magmatic patterns of HLP/SRP.

2. Overview: Post-20 Ma Pacific Northwest Volcanism

2.1 Geological Constraints

The Pacific Northwest has a long tectonic and geologic history [*Humphreys and Coblentz*, 2007], but our focus is on the last 20 Ma of magmatic evolution. Three volcanic features dominate this time period: the Columbia River/Steens Flood Basalts (CSFB), the High Lava Plains (HLP), and the Snake River Plain (SRP) [*Geist and Richards*, 1993; *Camp and Ross*, 2004] (Fig. 1). The CSFB is a voluminous pulse of basaltic melting and output beginning after 20 Ma and persisting beyond 15 Ma [*Swanson et al.*, 1979; *Carlson and Hart*, 1987; *Long et al.*, 2012]. Flood basalts surfaced through generally north-south trending dike swarms over a broad north-south region extending between ~42°N and ~48°N latitude, and lying roughly 500 km away from the trench and coincident with proposed region of plate extension [*Cross and Pilger*, 1978; *Eaton*, 1984; *Wells and Heller*, 1988]. Rough estimates for magma output during the flood basalt period range from ~200,000 – 450,000 km^3 [*Tolan et al.*, 1989; *Camp and Ross*, 2004]. Remarkably, it is estimated that ~98% of the magma volume was erupted in the first 2 Ma of activity [*Waters*, 1961; *Swanson et al.*, 1979; *Tolan et al.*, 1989; *Hooper et al.*, 2007].

The challenge for geochemical/geodynamic modeling of the post-20 Ma Pacific Northwest lies with the two, more recent east-west trending volcanic chains (HLP/SRP) lying to the south of the CSFB complex. The SRP volcanic track is less voluminous than the CSFB and records a striking age progression in rhyolitic volcanism [*Armstrong et al.*, 1975; *Humphreys et al.*, 2000; *Pierce et al.*, 2000; *Camp*

and Ross, 2004; *Jordan et al.*, 2004; *Smith et al.*, 2009]. This track is generally described as beginning near the McDermitt complex (~16 Ma) near the Oregon-Nevada border [*Malde*, 1991] or the south-western corner of Idaho (~12 – 14Ma) and extending north-eastward to the present day Yellowstone hotspot [*Camp and Ross*, 2004], with an estimated average eastward shift in felsic volcanic centers of 3 – 4 cm yr^{-1} [*Leeman*, 1982]. SRP volumetric rhyolitic output is estimated at 10,000 – 30,000 km^3 [*Ellis et al.*, 2013], an order of magnitude less than the CSFB. Important constraints on SRP formation come from seismic studies showing strong, low P- and S-wave velocity signals aligned with the SRP trend that are confined in depth (~200 – 300 km) and north-south extent (200 km) [*Schutt and Humphreys*, 2004; *Jordan*, 2005; *Waite et al.*, 2006; *Schutt et al.*, 2008]. Geophysical estimates attribute this confined shallow mantle structure to a modest excess temperature (50 – 120°C), 1 – 2% partial melt and a minor (0.25 mg s^{-1}) buoyancy flux [*Waite et al.*, 2005; *Schutt and Dueker*, 2008; *Smith et al.*, 2009].

Similar to the SRP, the HLP track records smaller volcanic output than the CSFB and exhibits an approximate trench-normal age progressive trend in rhyolites [*MacLeod et al.*, 1975; *Christiansen and McKee*, 1978; *Draper*, 1991; *Jordan et al.*, 2004]. Small volumes of rhyolitic magma, ~ 1,000 – 1,250 km^3 [*Ford et al.*, 2013], have erupted continuously from ~10 Ma to present day. The interesting twist is that the HLP felsic production youngs to the west, or opposite the SRP trend, at rates of between 3 cm yr^{-1} (11 to 5 Ma) and 1 cm yr^{-1} (5 Ma to present) [*Jordan et al.*, 2004]. HLP morphology is similar to the SRP with a less than 200 km wide track-normal expression in surface volcanism [*Draper*, 1991; *Jordan et al.*, 2004; *Meigs et al.*,

2009]. The mantle wedge beneath the HLP exhibits a somewhat confined slow seismic velocity anomaly that is weaker (2 – 4% dV_s/V_s) and less continuous along track than the SRP [*Long et al.*, 2012; *Wagner et al.*, 2012]. The stronger velocity reductions are resolved to a shallow 100 km thick section that appears laterally discontinuous beneath the HLP and broadens towards the western end of the HLP from 100 km to 200 km.

2.2 Melting Models

Though widely studied, the tectonomagmatic history of these three spatial-temporal events remain poorly understood and greatly debated [*Humphreys et al.*, 2000; *Hooper et al.*, 2007]. All modes of mantle melting and crustal growth have been proposed to explain the striking volcanic patterns in the Cascades, including subduction driven melting caused by mechanics of the Juan de Fuca plate beneath the North American plate [*Faccenna et al.*, 2010; *Liu and Stegman*, 2012], ridge melting due to back-arc extension [*Carlson*, 1984; *Carlson and Hart*, 1987; *Christiansen et al.*, 2002; *Long et al.*, 2012], and a Yellowstone mantle plume [*Morgan*, 1972; *Jordan et al.*, 2004; *Smith et al.*, 2009; *Kincaid et al.*, 2013]. Despite the complexity, this area provides an excellent setting for testing a spectrum of models for the style of upper mantle convection in convergent margins and the expected surface expression of related melt generation/transport processes.

Plume and non-plume models have been developed to reconcile the voluminous CSFB (~20 Ma), the age progressive (12 Ma to present) SRP volcanism that terminates at Yellowstone and the opposite, westward trending HLP volcanic track of central/eastern Oregon. There is presently intense ongoing debate on the plume model with the Pacific Northwest at one of the focal points for this dispute [*Foulger*, 2003, 2005; *Anderson and Natland*, 2005; *Foulger et al.*, 2005]. A plume, or thermally buoyant mantle upwelling with a flood basalt producing head and long-lived tail for generating an eastward progressive track, is commonly cited as the key dynamic process for CSFB and the age progressive rhyolitic volcanism of SRP

[*Richards et al.*, 1989; *Camp and Ross*, 2004; *Pierce and Morgan*, 2009; *Smith et al.*, 2009]. But the equivocal HLP, whose rhyolite lavas young opposite North American plate motion, and the north-south offset between CSFB and SRP is inconsistent with the simple plume model [*Christiansen et al.*, 2002].

A non-plume model has also been considered to explain the volcanic patterns of the PNW. Supporters of a non-plume theory invoke plate motions to trigger large-scale melting events, like the CSFB [*Faccenna et al.*, 2010; *Liu and Stegman*, 2012; *Long et al.*, 2012]. Geodynamic 3D models have shown that changes in slab motions (e.g. subduction initiation, rollback initiation or acceleration, and slab steepening) can result in an upward mantle circulation (i.e. a proxy for decompressional mantle melting) in the wedge [*Kincaid and Griffiths*, 2004; *Long et al.*, 2012]. *Long et al.* [2012] propose that the voluminous CSFB melting event was a direct consequence of JdF slab rollback initiation ~20 Ma and subsequent back arc-extension. This work further suggests that later stage melting (12 Ma – present day) in the mantle beneath HLP could be a result of a rollback-controlled wedge circulation (i.e. toroidal flow), continued upwelling in the wedge, and thinning of the lithosphere. But this non-plume model and others fall short in explaining the SRP-Yellowstone track and concurrence and unique progression of HLP/SRP.

Whether the CSFB event was the result of plume activity or upper mantle melting driven by plate mechanics, geodynamic studies have yet to address the fate of the flood basalt residuum beyond schematic cartoon models depicting its influence on mantle circulation [*Humphreys et al.*, 2000; *Smith et al.*, 2009]. Results are presented

from a series of geodynamic laboratory experiments designed to test the importance of the CSFB mantle residuum on 4D circulation, transport, and melt production.

3. Laboratory Methods

3.1 Apparatus

We examine the evolution and interaction of mantle chemical heterogeneity, or residuum, in 4D subduction-driven flow using a kinematic laboratory model [e.g., *MacDougall et al.*, 2014]. The mantle is modeled using glucose syrup, i.e. a Newtonian viscous fluid, in a transparent Plexiglas tank (150 cm long × 75 cm wide × 45 cm deep). Similar to *Hall and Kincaid* [2001], the subducting slab is modeled by reinforced continuous rubber belts moving around rollers (Fig. 2a). A large percentage of the wedge superadiabatic thermal gradient is locked up in the subducting plate. Thus, the downgoing slab is expected to be the dominant driver of forced convection in the upper mantle. While dynamic subduction of a tabular plate is ultimately the goal for wedge circulation studies, there remain a large number of poorly constrained processes in these models (e.g., rate of convection and upwelling in the mantle wedge, shear stress on the base of the lithosphere, etc.). We choose kinematic models because forced convection of the wedge can be generated in a reproducible fashion.

We employ kinematic subduction modeling where precise downdip (U_D) and translational, i.e. trench retreat, (U_T) motions of the slab are prescribed to mimic slab motions observed in 3D, time-evolving dynamic subduction models [*Kincaid and Olson*, 1987; *Griffiths et al.*, 1995; *Funiciello et al.*, 2003, 2006; *Schellart*, 2004]. An advantage to using kinematic subduction modeling is that each experiment is repeatable and controllable. In this way we are able to characterize the wedge response to mantle heterogeneity in 3D wedge flow fields when key parameters in plate

mechanics are varied. The glucose syrup used to model both upper mantle and residuum is a Newtonian viscous fluid with temperature dependent viscosity, described by *Olson and Kincaid* [1991]:

$$\mu(T) = exp\left(\frac{1888}{T+93.3} - 11.48\right) \quad (1)$$

where μ and T are dynamic viscosity (Pascal-seconds) and temperature (°C), respectively. The volume of fluid (4.5×10^5 cm^3) representing the ambient mantle is maintained at a constant temperature, resulting in isothermal density of 1.42 g cm^{-3} and dynamic viscosity of 134 Pa·s at 22°C. The mantle wedge is isothermal until it interacts with the mantle residuum, a thermally altered patch of glucose syrup. The volume of the residuum is 200 cm^3 for all experiments, while temperature (T_R), thereby viscosity (μ_R), is varied. For visualization purposes the mantle heterogeneity is marked with neutrally buoyant red tracers (beads, whiskers) and micro-bubbles that distinguish it from the ambient mantle fluid, which is laced with white whiskers. These passive Lagrangian flow tracers move with the fluid providing velocity information in both space and time throughout the course of the experiments.

We model three distinct styles of overriding plate in our experiments. In the first setup, we assume a decoupling zone exists between mantle and overriding lithosphere. These experiments have a free slip mantle surface, in which the mantle surface moves independently of upper plate motion. Our second set of models use a strongly coupled mantle-lithosphere boundary to create a no slip mantle surface condition. In these cases a uniform overriding plate (OP) is modeled using a thin, transparent Plexiglas plate that migrates with trench motion. The OP couples with the underlying wedge fluid, imposing a vertical shear flow under the plate (Fig. 3a). In the

third set of overriding plate models we simulate extension in the back-arc (BAE) using mylar sheeting along the fluid surface (Fig. 3b). The extension center moves at the prescribed trench migration rate (U_T). As the trench retreats, mylar spools from a reel to the extensional axis in the back-arc. The mylar couples with the underlying fluid east of the extension center and imposes a zero horizontal surface velocity on the wedge surface.

3.2 Scaling

The length and time scales of these kinematic models, representing dynamic sinking modes, are scaled to the mantle using a dimensionless ratio of advective to diffusive heat transport, written as the Péclet number,

$$Pe = \frac{U_D L}{\kappa} \quad (2)$$

where length scale, L, is defined as the width of the trench (L_{lab} = 25 cm, L_{mantle} = 1625 km) and the thermal diffusivity (κ) values for lab and mantle are 10^{-3} and 10^{-2} cm^2 s^{-1}, respectively. Time and velocity scales are calculated by relating laboratory and mantle Péclet numbers. Thus, a U_D of 1 cm min^{-1} in the lab relates to 0.8 cm yr^{-1} when scaled to the Earth's mantle and 1 min in the lab corresponds to ~8 Ma of geologic time.

3.3 Experimental Methods

The experimental method for melt residuum experiments has been developed through the running of over 60 distinct cases. Experiments begin after the placement of mantle heterogeneity on the surface of the upper mantle wedge, i.e. our experiments begin after a major melting event resulting in creation of the flood basalt residuum.

A residuum volume of ~200 cm^3 scales to an initial melt residuum volume of 5.5×10^7 km^3. We assume a residuum volume ~10 times larger than the combined estimated erupted and unerupted magmas extracted from the mantle during the CSFB melting event. Rough estimates for magma output during the Cascades flood basalt period range from ~200,000 – 450,000 km^3 [*Tolan et al.*, 1989; *Camp and Ross*, 2004]. We also consider that the solidified magma intrusions beneath a large igneous province can represent a substantial unerupted igneous volume [*Crisp*, 1984; *Walker*, 1993; *White et al.*, 2009]. Thus, when determining the initial size of our CSFB melt residuum, we estimate a 10% mantle melt fraction represented by surface lavas and unerupted, underplated magmas.

The laboratory residuum is made from the same glucose syrup as the ambient wedge fluid. Temperature differences are used to represent a wide range in residuum viscosity contrasts. Heterogeneity temperature, i.e. viscosity, is an experimental variable. To create the low or high viscosity heterogeneity we heat or chill the glucose syrup, respectively.

After the heterogeneity is brought to the appropriate temperature, it is placed in the wedge. Location in map view is most often centered in the wedge about the slab

centerline and ~14 cm (~900 km) from the trench (e.g. location 'A', Fig. 2c). The heterogeneity is approximately oval shaped, long in the trench-parallel direction, ~20 cm (~1300km), and constrained in the trench-normal direction, ~5 cm (~325 km). While we can control heterogeneity volume, temperature, and general location, once the residuum is placed in the wedge, natural viscous effects take place prior to experiment initiation. Our low viscosity heterogeneity has a viscous puddle spreading speed of ~0.4 cm min^{-1} when placed in ambient mantle fluid. So naturally less viscous heterogeneities spread more and tend to occupy more surface area than more viscous heterogeneities when placed in the tank. Likewise, less viscous heterogeneities extend to shallower depths (~2.5 cm, corresponding to ~165 km in the mantle), while more viscous heterogeneities reach to deeper depths (~ 3.5 cm, ~225 km). Thus, there are slight initial morphology differences at the initiation of each experiment.

In the following cases, and throughout the paper, we use the terminology "weak" or "strong" heterogeneity to relate the strength, or viscosity, of the residuum (μ_R) to that of the surrounding mantle (μ_M). The viscosity ratio, $\mu^* = \mu_R/\mu_M$, is used to determine whether the residuum is weak ($\mu^* < 1$) or strong ($\mu^* > 1$). We assume that the strength of the flood basalt residuum is determined by the mantle's ability to retain partial melt and volatiles after the CSFB event. In the case of strong residuum we assume eruption of melt and volatiles to the surface results in a more viscous chemically altered heterogeneity [*Jordan*, 1975, 1978; *Pollack*, 1986; *James et al.*, 2001]. Following a similar logic, a low viscosity heterogeneity results from the mantle's capacity to stably hold some partial melt at shallow mantle depths [*Hirschmann*, 2010]. Though P and S wave velocity anomalies can detect the presence

of retained melt in today's upper mantle [e.g., *Toomey et al.*, 1998; *Villagómez et al.*, 2014], dV_P and dV_S data only offer a present day snapshot. Since we are unable to determine the residuum viscosity resulting from a melting event that occurred millions of years ago, e.g. CSFB at ~20 Ma, we model both end members ($\mu^* < 1$ and $\mu^* > 1$) in each set of experiments.

Assuming that the residuum creation occurs at ~20 Ma and that the experimental time begins at $t^* = 0$, we monitor the wedge flow-residuum interaction through present day (0 Ma), $t^* = 1$ or 2.5 minutes of laboratory time. To understand the long-term wedge impact we run the experiment 60 Ma into the future (up to $t^* = 4$ or 10 minutes in the lab). All plate motions initiate at the beginning of the experiment ($t^* = 0$). Throughout the length of the experiment, slab downdip (U_D) and trench translational rollback (U_T) rates are 8 and 3 cm min^{-1}, which correspond to mantle values of 6.5 cm yr^{-1} and 2.4 cm yr^{-1}, respectively. We model an intermediate slab dip angle (θ) of 50° from horizontal in all cases.

Inertial effects are neglected for all experiments. The Reynolds number, *Re*, for the laboratory fluid is defined as,

$$Re = \frac{\rho u D}{\mu} \quad (3)$$

Reasonable values for the laboratory glucose syrup are $\rho = 1.42$ g cm^{-3}, $D = 40$ cm is the depth of the tank fluid representing the mantle, $u = 8$ cm min^{-1}, and $\mu = 134$ Pa·s. The Reynolds number for our laboratory model is calculated to be $Re = 5.6 \times 10^{-3}$. Thus our analogue mantle fluid with $Re < 1$ is largely unaffected by inertia and flow is laminar.

With the high viscosity heterogeneity present in the shallow wedge, the system is unstable and convects. Using the formula for the onset time of a residuum-ambient fluid boundary layer instability from *Olson* [1990]:

$$\tau = \frac{1}{\pi\kappa^{1/3}} \cdot \left(\frac{\upsilon Ra_c}{\alpha g \Delta T}\right)^{2/3} \quad (4)$$

where Ra_c is the critical Rayleigh number, υ is the dynamic viscosity, g is gravity, ΔT is the maximum temperature rise between the ambient fluid and residuum, and κ and α are thermal diffusivity and thermal expansivity of the lab fluid, respectively. Reasonable values of $Ra_c = 3 \times 10^3$, $\upsilon = 10^3$ cm^2 s^{-1}, $g = 9.8$ m s^{-2}, $\Delta T = 9$ K, $\kappa = 10^{-3}$ cm^2 s^{-1}, and $\alpha = 4.5 \times 10^{-4}$ K^{-1}, gives $\tau \sim 7$ hours, the amount of time for Rayleigh-Taylor instability onset on the underside of the most viscous residuum. Using the scaling indicated by the Péclet number we determine that the diffusion characteristic timescale for corn syrup with thermal diffusion distance of 1 cm is ~17 minutes, almost twice the length of a typical experiment. Subsequently, residuum buoyancy and thermal diffusivity are second order factors over the duration of an experiment.

Our length scale is defined by the width of the trench (~1625 km) which is larger than the current width of the Juan de Fuca trench, ~1200 km. Plate tectonic reconstructions [e.g., *Atwater*, 1970; *Atwater and Stock*, 1998] show that over the last 25 Ma the Cascadia slab width has been decreasing with the northward migration of the Mendecino triple junction. Calculations of the Pacific-North American plate reconstructions estimate that the 20 Ma Cascadia plate boundary extended as far south as 35°N [*Atwater and Stock*, 1998], resulting in a subducting slab ~2000 km wide. In our lab model, with approximate representation of a system with complex spatial-temporal characteristics, the subducting plate maintains a fixed width throughout the

experiment. In order to account for the diminishing width of the Cascades slab over the last 20 Ma, we model an average slab width over this time period of 1625 km.

3.4 Data Collection

Data on deformation and entrainment of mantle heterogeneity in subduction-induced flow are collected throughout the experiment duration using high-resolution digital photography. Two cameras are used to take side view and map view photographs of flow illuminated in two alternating light sheets. A vertical light sheet illuminates the fluid along the slab centerline for side view imagery and a horizontal light sheet illuminates a fluid depth of ~1 cm for map view imagery. The horizontal light sheet is ~1 cm thick and starts ~1 cm beneath the lab fluid surface, thus all experiment map view images highlight flows from a mantle equivalent depth range of ~65 – 130 km. Spatially detailed (± 5 mm), time lapsed photographs are taken every 5 seconds to capture wedge evolution through time. Cameras move with the subduction apparatus at trench migration rate (U_T) so map and side view perspectives are in a fixed trench reference frame. Digitizing software (*GraphClick*) is used to track passive micro-tracers in the wedge. Lagrangian particle velocity is calculated by dividing the digitized distance traveled by the known time interval between successive frames. Fluid flow patterns represent material pathlines in a fixed trench reference frame. Throughout this paper, all velocities and flow directions are given in a fixed trench reference frame. For more information on how reference frame affects observed wedge flow fields see the Supplemental Information.

4. Experimental Results

Using a subset of 15 experiments (Table 1), we investigate the role of upper mantle heterogeneity in subduction systems. We develop qualitative and quantitative relationships between the subducting plate style, overriding plate structure, wedge flow fields, and melt residuum transport and deformation. In each case we characterize the time dependence and distribution of material transport in the wedge and compare these data to the seismologic results, geochemical data, and post-20 Ma surface tectonomagmatic activity of the PNW.

4.1 Time Evolution of Residuum: Rollback Subduction

The first set of experiments model a free slip surface, i.e. we model mantle decoupling from the overriding lithosphere. Results show that wedge return flows are highly 3D and the addition of a rheological heterogeneity disturbs basic flows. Fig. 4 highlights the evolution of a rollback experiment where the slab subducts with downdip (U_D = 8 cm min^{-1}) and translational rollback (U_T = 3 cm min^{-1}) motions. All images are shown in a fixed trench reference frame.

The weak heterogeneity (Exp. 6, μ^* = 0.3) experiences pure shear in transformation from an initial north-south morphology to an east-west morphology after 2.5 minutes (~20 Ma) (Fig. 4a – c). Rollback induced toroidal flow moves fluid around the slab edges into the wedge from the north and south at rates of ~4.0 cm min^{-1} (~0.50U_D) which efficiently compresses the residuum towards the slab centerline (Fig. 4b – c). Concurrently, subduction zone corner flow draws residuum and ambient wedge fluid towards the trench at velocities of ~3.5 cm min^{-1} (0.44U_D). Slab entrainment velocities decrease with distance from the trench. The far eastern edge of the residuum migrates towards the slab at an average rate of ~1.0 cm min^{-1} (0.14U_D). At t^* =1 (~1.25 min into the experiment) the leading edge of the residuum is at the trench and will begin subducting from the shallow mantle. Later stage images of this case (Fig. 5a – b) reveal the long-term fate of weak heterogeneity in the subduction system. After 10 minutes (~80 Ma or t^* = 4) most of the initial residuum volume has subducted (estimated ~95%), but a very small amount (~5%) has not flushed from the shallow wedge. Over this time period the low viscosity feature shows continued

trench-parallel thinning; with a trench-parallel width of < 1 cm (~ 50 km), extending along the slab centerline. This narrow band of low viscosity fluid remains in the wedge for the duration of the experiment and has > 80 Ma expected lifetime in the shallow wedge.

Changing residuum μ^* affects mass and energy transport within the wedge, on both short and long-term timescales. Fig. 4d – f illustrates the ~20 Ma evolution of a strong (i.e., high viscosity) heterogeneity in a rollback experiment (Exp. 5, $\mu^* = 8$). All model parameters remain the same from Exp. 6 except for the viscosity contrast (μ^*). Similar to the weak heterogeneity, slab entrainment translates the strong heterogeneity towards the trench and U_T-induced toroidal flow results in north-south compression towards the slab centerline. Unlike the low viscosity wedge feature, which experiences pure shear as it deforms into an east-west trending morphology, the high viscosity feature resists internal deformation and instead folds along the trench-normal symmetry line (Fig. 4e – f). The strong residuum is more resistant to the deformation flows coming from the north and south edges at rates of ~3.5 cm min^{-1} (~0.44U_D). Unlike the low viscosity heterogeneity which compresses down to ~6 cm (~390 km) in trench-parallel width, the more viscous morphology maintains 55% of it's initial north-south length and at 20 Ma has a trench-parallel length of ~11 cm (~715 km). Another striking dissimilarity between variable μ^* cases is the residuum entrainment style. With strong heterogeneity present in the wedge, the entire feature is entrained towards the trench as one block. This feature translates at ~2 cm min^{-1} (~0.23U_D) which is a slower rate than the weak residuum. By present day it is still ~4 cm (~260 km) from the trench. At later stages of evolution, efficient entrainment of viscous

heterogeneity results in ~95% of the heterogeneity flushing from the shallow mantle wedge over 80 Ma (Fig. 5c – d), and 100% by 90 Ma. So while both strong and weak heterogeneities result in ~95% of the residuum being subducted after 80 Ma, the behavior of the remaining 5% of the residuum typifies the varying reactions of the residuum to the flow fields produced in the wedge by the different tectonic drivers.

Circulation in the form of return flows into the innermost wedge is strongly influenced by the presence of viscous heterogeneity. Average instantaneous velocity and particle direction are summarized in 3 distinct wedge regions: slab centerline, northern edge, and mid-region (Fig. 6). For each zone, instantaneous non-dimensional velocity is defined as U_M/U_D, where U_D is the slab convergence rate (8 cm min^{-1}) and

$$U_M = \sqrt{{v_x}^2 + {v_y}^2} \quad (5)$$

where v_x , trench-normal velocity, and v_y, trench-parallel velocity, are calculated using *x*, *y*, and *t* data collected from digitizing software *GraphClick*. Normalized particle flow direction (Φ^*) in a fixed trench reference frame is also calculated from this data. Fluid migration direction, Φ^*, ranges from 1 to -1, where $\Phi^* = 1$ represents westward (trenchward, trench-normal) velocities, $\Phi^* = 0$ for southward (trench-parallel) flows, and $\Phi^* = -1$ for apparent eastward (away from slab, trench-normal) directional flows. We calculate instantaneous U_M/U_D and Φ^* for particles located in the ambient fluid and residuum at three times: experiment initiation ($t^* = 0$ or 20 Ma), at 1.25 minutes ($t^* = 0.5$ or 10 Ma), and at 2.5 minutes ($t^* = 1$ or present day); then average over different regions. We confine our analysis to the northern wedge; our simplified model is symmetric about the slab centerline so we observe mirrored flow patterns about the slab centerline in the southern wedge. To isolate the impact of

heterogeneity in rollback subduction, Fig. 6 compares average instantaneous velocity, U_M/U_D, and direction, Φ^*, in the northern (black), mid (blue), and central (red) regions of the wedge (see Fig. 6a for location boundaries) for weak and strong heterogeneity present in the wedge (Exp. 6 and Exp. 5, respectively).

There are basic similarities in wedge circulation, along with key differences, when a weak versus strong residuum is present. Regardless, flow enters the edge of the wedge in the north to south direction and near the slab centerline transitions to fully east to west, trench-normal, approach velocities (Fig. 6b). On average, there is a gradual transition from trench-parallel to trench-normal flow through the mid-region of the wedge. Trench parallel flow rates entering the edges of the wedge reach ~$0.55U_D$ with a weak residuum and slightly reduced rates, ~$0.50U_D$, when a strong residuum is present (Fig. 6c). Average trench-normal flows in the central wedge (red region) are inversely related to distance from the trench though mean velocities are slower, reaching ~$0.45U_D$ when $\mu^* < 1$ and ~$0.35U_D$ when $\mu^* > 1$ (Fig. 6e).

There are, however, a number of important differences in detailed flow structure based on viscosity of the residuum. Moving trenchward (from east to west) the greatest increase in U_M (+$0.30U_D$) is seen in the wedge with weak heterogeneity. With a high viscosity residuum in the wedge, slower slab centerline velocities supply mass to the trench (Fig. 6e). Activated return flows show up in greater U_M increases in the northern edge and mid-region when a strong heterogeneity is present in the wedge (Fig. 6c, d). Values for U_M in the strong residuum case show trenchward increases of +$0.15U_D$ and +$0.05\ U_D$ over the weak residuum case in the northern edge and mid-region, respectively (Fig. 6c, d).

Across all regions, average velocities in the shallow wedge are reduced when a strong heterogeneity is present (Fig. 6c – e). Exp. 6 and Exp. 5 have the same prescribed slab motions (Table 1), but in the strong residuum case the wedge heterogeneity slows down the ambient fluid existing in the same x-y plane. In our analysis of x-z plane residuum evolution (Fig. 10a,b and 11a), we observe that with a high viscosity plug slowing surface flows, sinking velocities increase to feed the subduction system.

4.1.1 Effect of an Overriding Plate

Surface flow coupling to an overriding plate is important for full wedge circulation results. Two end member wedge surface conditions exist: fully coupled and fully decoupled. Experiments in the previous section have a free slip surface condition, i.e. decoupled. In the free slip mantle end member condition we assume that the non-Newtonian rheology of the mantle [*Hirth and Kohlstedt*, 2003] and increased amount of shear at the lithosphere/upper mantle boundary result in decreased viscosity and decoupling of shallow mantle from the overriding lithospheric plate [e.g., *Jadamec and Billen*, 2012]. In our next set of experiments we assume that the upper mantle cannot move independently of the overlying lithosphere. The addition of an overriding surface plate (OP) changes the time-dependent flow generated by the subducting slab and greatly impacts the residuum evolution. We model the overlying lithosphere using a clear Plexiglas plate that sits on the fluid surface and moves with the trench at slab translation rate U_T (Fig. 3a). The OP couples with the underlying wedge fluid, imposing a vertical shear flow under the plate.

Map view Lagrangian particle velocities in a fixed trench reference frame are calculated for an ambient wedge with free slip (Exp. 2) and no slip (Exp. 3) mantle surface conditions (Fig. 7). Parameters in both cases are the same except for the presence of the overriding plate in Exp. 3 (Table 1). The OP influences material and flushing time scales of the fluid in the shallow upper mantle. U_T-induced toroidal flow decreases by ~$0.2U_D$ on the wedge north and south edges and entrainment velocities decrease up to ~$0.3U_D$ when the system includes a no slip surface condition. In a fixed

trench reference frame, flow direction is approximately the same in Exp. 2 and Exp. 3. However, in an absolute reference frame flow orientation does change with presence of an OP. For more information on how reference frame affects observed wedge flow fields see the Supplemental Information.

Lagrangian particle pathline velocities in the vertical (x-z) plane illustrate the same pattern of decreased entrainment velocities in the upper 2 cm (130 km) of the wedge with introduction of an OP (Fig. 8). Average U_M/U_D in the uppermost wedge fluid show an OP imposed vertical shear flow under the plate (Fig. 8c). Slight upwelling velocities ($\boldsymbol{v_z}$ up to 0.06 cm min^{-1}) created by the shear-induced net upward torque are observed in the shallow wedge (Fig. 8b). Though the upper ~2 cm of the mantle flow is dampened by the presence of a fully coupled surface, Fig. 8c shows that deeper in the wedge velocities increase. Between 2 and 3 cm depth, average velocities in the experiment with fully coupled surface are greater than average U_M with decoupled mantle surface. This suggests that activated return flows providing mass for subduction are originating from depth.

The introduction of a no slip mantle surface also results in viscous coupling to the base of the lithosphere in experiments with heterogeneity. Surface coupling to the base of a lithospheric plate dampens the residuum north-south deformation rate (Fig. 9). Initial north-south residuum length L_0 = 20 cm, corresponds to 1300 km when scaled to the mantle. A weak heterogeneity experiences the greatest trench-parallel deformation over a 40 Ma (5 minute) evolution. By t^* = 2, low viscosity residuum has changed north-south extent dramatically (~0.1L_0) with no OP and moderately (~0.5L_0) when the wedge couples to an OP. This is consistent with 3D flow rates in Fig. 7. A

strong residuum located in the wedge is more resistant to slab induced deformational flows. After 5 minutes (40 Ma) evolution, a high viscosity feature maintains ~0.3L_0 with no OP and ~0.95L_0 with OP. The decrease in trench-parallel deformation in cases with overriding plate is the result of two factors: (1) introduction of an overriding plate dampens U_T-induced toroidal near-surface flows (Fig. 8b, c); and (2) residuum, especially $\mu^* > 1$, viscously couples to the base of the OP and resists deformation (Fig. 9b).

Results indicate that slab-induced upper mantle circulation can deform and entrain wedge heterogeneity. We've shown that a weak heterogeneity decoupled from the overriding plate most easily deforms from a trench-parallel (north-south) morphology to a trench-normal (east-west) morphology, over 20 Ma time scales. However, an additional first order feature of volcanism needs to be considered, namely melt production patterns. These include volumetric trends and age progressions in the lavas, e.g. the CSFB event produced 200,000 – 450,000 km^3 [*Tolan et al.*, 1989; *Camp and Ross*, 2004] while the SRP eastward trending and the HLP westward trending rhyolitic volumetric output is estimated at 10,000 – 30,000 km^3 [*Ellis et al.*, 2013] and 1,000 – 1,250 km^3 [*Ford et al.*, 2013], respectively. To access vertical velocity, we consider flow and deformation patterns in side view for cases of different μ^* and surface condition (Fig. 10).

Side view analysis provides insight on the slab entrainment and transport of μ^* residuum from shallow mantle to deep (Fig. 10 a, b). At $t^* = 1$, the less viscous heterogeneity resembles a thin vertical sheet that runs along the slab centerline (e.g., Fig. 4c) and extends from mantle surface to depths beyond the shallow mantle (Fig.

10a). Comparatively, analysis of the vertical plane with strong residuum present shows that the feature is fully entrained and the entire mass approaches the trench (Fig. 10b), similar to the map view observation (e.g., Fig. 4f). To compensate for slower shallow mantle velocities when strong heterogeneity is present (Fig. 6), deeper mantle is sourced for subduction. In our x-y plane velocity analysis (Fig. 6c – e), strong residuum in the wedge results in slower circulation throughout the shallow mantle horizontal plane (z ~1 – 2 cm). In the x-z plane, the greatest sinking velocities, up to 0.5 cm min^{-1}, occur when a high viscosity feature is present in the wedge (Fig. 10b). In comparison, weak heterogeneity experiences greater flow velocities in the shallow wedge x-y plane (Fig. 6c – e) and slower sinking velocity, ~0.3 cm min^{-1}, in the vertical plane (Fig. 10a). Thus, the relative intensities of entrainment and sinking velocities supplying the mass for subduction varies based on μ^* heterogeneity present in the shallow mantle wedge.

Residuum couples to the no slip surface when an overriding plate is introduced (Fig. 10c, d) producing a significant decrease in sinking velocities. Weak heterogeneity tends to remain in the shallow mantle wedge, adhered to surface plate, until coupling occurs with the subducting slab (Fig. 10c). More viscous heterogeneity strongly adheres to the underside of the OP and experiences limited deformation and entrainment over 2.5 minutes or 20 Ma when scaled to the mantle (Fig. 10d). There is slight shear-induced upwelling detected beneath and on the western side of the residuum in each case. Vertical rise velocities up to ~0.2 cm min^{-1} (weak heterogeneity) and ~0.1 cm min^{-1} (strong heterogeneity) are observed along the deep

and western residuum-ambient fluid interface. However, no evidence of vertical motion exists on the eastern side of the heterogeneity.

Long-term flux of rheological heterogeneity to the deep system is highly dependent on μ^* and fluid surface coupling conditions (Fig. 11). With no OP, the estimated volumetric flushing time for weak and strong heterogeneity is approximately the same (Fig. 11a). A strong residuum in a system with a decoupled fluid surface (e.g., Exp. 14), μ^* is strongly entrained down with the subducting slab. 98% of the heterogeneity is flushed from the shallow wedge to depths greater than ~3 cm (~200 km) by $t^* = 3$, corresponding to 60 Ma when scaled to the Earth (Fig. 11a). The remaining 2% is strongly entrained, meaning the high viscosity residuum will completely flush from the wedge within the next 5 Ma resulting in a total shallow wedge lifetime of ~65 Ma. The majority of the low viscosity residuum volume subducts as well (~90% in 60 Ma) (Fig. 11a). However, a thin vertical sheet of residue is not strongly entrained (e.g. Fig. 5a – b). Late stage results show that low viscosity features, though thin, are a long-lived (over 80 Ma) source of chemical heterogeneity in the wedge.

Deformation and entrainment patterns of wedge heterogeneity alter drastically when an overriding lithospheric plate is added to the model (Fig. 11b). Over 60 Ma, strong residuum lying beneath an OP experiences slight deformations and entrainment. But due to strong viscous coupling with the overlying lithosphere, only 6% of the residuum volume has downwelled below the shallow mantle. ~83% of the weak residuum with fully coupled mantle surface has flushed by $t^* = 3$. The remaining 17% exists in a thin horizontal sheet that is coupled to the no slip surface. Here, and in the

case with no OP, low viscosity heterogeneities are capable of long lifetimes in the mantle wedge. Thus weak residuum has the greatest potential to impact wedge chemistry over long timescales.

4.1.2 Effect of Back-Arc Extension

Results so far show how simple plate motions give rise to evolving 3D flow fields that affect residuum deformation and evolution, but so far residuum cases have not produced complex upwelling patterns. Although our decoupled versus coupled wedge surface results show strong differences in vertical velocity, these upwelling patterns do not match a number of key characteristics of Cascades, e.g. HLP/SRP thin tracks with opposite age progressive lavas. An essential condition of the Cascadia subduction system that we will be modeling is the introduction of back-arc extension (BAE) above the mantle wedge [*Wernicke et al.*, 1988]. BAE cases are crucial in linking our model results to post-20 Ma observations of the PNW. The interaction of 4D circulation and heterogeneity impacts flow patterns, thereby influencing wedge melting processes and surface volcanism.

The addition of BAE provides a mechanism for upwelling related decompression melting in the shallow wedge. The extension center moves at prescribed trench migration rate (U_T) in our simplified subduction model. The extensional axis separates the arc plate (AP) in the west from the overriding plate (OP) to the east. As the axis translates horizontally, Mylar spools out at the extension location (Fig. 3b). The stationary OP imposes zero horizontal velocity on the mantle surface below. The AP has a free-slip mantle surface condition and extends from the trench to the BAE axis located ~13.5 cm, ~900 km, from the slab. The OP extends from the extensional axis to the far eastern edge of our model. Low viscosity (Exp. 27)

and high viscosity (Exp. 18) heterogeneities representing flood basalt residua are placed in the central wedge at experiment initiation (Fig. 12)

The presence of an extensional axis provides a dramatic return flow regime boundary for material reaching the areas beneath the arc volcanics and the wedge apex. The subducting slab does not entrain residuum and ambient fluid located east of the extension center as both trench and extensional axis translate westward at rates of 3 cm min^{-1} (Fig. 12). Heterogeneities adhere to the OP, which is stalled relative to the system rollback, and are left behind at ~ 2 cm min^{-1} (Fig. 12b, e). Wedge material located beneath the AP, i.e. trenchward of the BAE axis, is entrained towards subduction. East-west extension (in the trench-normal direction) occurs along the length of the heterogeneity due to the increasing gradient in trench-normal approach rates.

Horizontal velocities for a weak heterogeneity located beneath the AP reach ~3 cm min^{-1}. Between 10 and 0 Ma ($t^* = 0.5 – 1$), the low viscosity feature separates into two unconnected entities (Fig. 12c). The space between the two discrete features grows with time as the subduction system moves west and the detached residuum beneath the OP is left in the east. Exp. 18 illustrates the strong heterogeneity stress guide effect. Due to viscous coupling within the strong heterogeneity, slab-ward advection of residuum beneath the AP is limited (Fig. 12d – f). Approach velocities of the western side are ~1 cm min^{-1}, or only ~30% of the rates for the weak heterogeneity case (Fig. 12b). After 20 Ma, the strong heterogeneity remains intact and robust from west to east (Fig. 12f).

Complex 4D flow fields emerge when upper plate extension is modeled. In respect to the trench, wedge material beneath the overriding plate has an average southeast to east flow direction across all zones (Fig. 13b, c). East of the extension axis, surface fluid is not entrained for subduction ($\Phi^* < -0.3$). The presence of BAE results in efficient return flows along the northern edge of the wedge. The fastest average fluid velocities, ~$0.55 – 0.65U_D$, occur in the shallow wedge beneath the AP at the northern edge (Fig. 13d). High U_M trench parallel flows ($\Phi^* \sim 0$) are transporting mass southwards, from wedge edge to centerline. These activated return flows result in order to compensate for the mass no longer sourced for subduction from the far eastern side of the wedge.

As in previous cases, despite the presence of BAE circulation in the wedge is sensitive to a mantle heterogeneity located beneath the extension location. On the northern edge region (Fig. 13a, black zone) and mid-region (Fig. 13a, blue zone) there is limited residuum presence during the course of the experiments. Between cases average U_M and Φ^* are similar within each zone. As previously discussed, fast trench-parallel flows exist on the northern edge. Moderate (~$0.35U_D$), westward trench-oblique particle motion exists on the mid-region (Fig. 13e). There is a greater residuum presence along the slab centerline. In the red zone flows readily reorient to a trench-normal direction from east to west. Wedge flow in this region reorients at a slower rate when strong residuum than when weak residuum is present (Fig. 13c). Slab centerline U_M is the same for both cases beneath the OP. Beneath the AP, weak heterogeneity experiences faster average slab-ward velocities (~$0.35U_D$) than the case with the strong heterogeneity (~$0.25U_D$) (Fig. 13f).

Investigation of heterogeneity evolution in side view further highlights the importance of μ^* features in 4D upper plate-driven wedge (Fig. 14a, b). As we saw in map view, the weak residuum splits into two distinct features while the strong heterogeneity remains intact. Exp. 27 (low viscosity residuum) is distinct in that the ambient fluid-residuum interface is slanted and shallows with time (Fig. 14a). Along the slab centerline, upwelling is detected in the shallow wedge along the residuum interface boundary with the fastest rise velocities (up to ~0.05 cm min^{-1}) seen, as expected, beneath the extensional axis (Fig. 14c). The strong heterogeneity is robust directly beneath the BAE location (Fig. 14b). Maximum vertical velocities (up to ~0.05 cm min^{-1}) are resolved within and up the eastern side of the viscous plug (Fig. 14c). In both cases shallow wedge velocities are beginning to downwell ($v_z < 0$) near the trench due to the downward entrainment of the slab. However, vertical rise velocities still exist in the shallowest portion of our domain-averaging window (Fig. 14c, representing the region between mean and one standard deviation above the mean).

Results reveal interesting horizontal versus vertical flow dominant regimes indicating that upwelling patterns depend not only on residuum presence but also on location within the wedge. It is only along the slab centerline that trench-normal approach velocities, that are less than downdip subduction rate, must be compensated for by an advected vertical velocity. Here, material must be brought up from deep, against gravity, to fill in the mass deficit created by the extension center on the surface. Away from the central wedge flow is predominantly horizontal toroidal flow,

with little vertical component. Thus, model predictions indicate that melting will be constrained on trench-normal tracks on the slab centerline.

Analysis of μ^* residuum deformation beneath the BAE axis reveals that it is possible to produce age-progressive mantle melting. As previously discussed, we confine the greatest upwelling to central wedge, along the trench-normal, slab centerline track. Relative strength and chemical composition of the residuum beneath the back-arc extension axis will effect upwelling related decompression melting trends (Fig. 14). The interface represents a boundary between the more refractory residuum and ambient mantle. As it shallows and migrates, this boundary controls both the chemical composition and timing of the resulting partial melts (Fig. 15).

Different wedge upwelling patterns occur when heterogeneity viscosity is varied (Fig. 14). Shallowing of residuum and ambient fluid throughout the top 3 cm (200 km) creates a decompression melting favorable environment. An essential point however is that not all wedge upwelling will produce decompression melting. Melt production will be delayed in rising residuum parcels that have experienced prior melt extraction and are more refractory, with a solidus that is shifted towards higher temperatures. Focusing in on the residuum-ambient fluid interface, this results in a different melt onset times for neighboring parcels. Melting will depend not only on a particle's ability to rise but also on its composition, location in P-T space, and wedge potential temperature (Fig. 15a). In our analysis we assume a fertile mantle lherzolite composition for the ambient mantle and a refractory harzburgite composition for the depleted mantle residuum. Using these assumptions, ambient mantle will start to melt at depths between ~75 and 20 km for wedge potential temperatures of 1500 and

1300°C, respectively (Fig. 14d). Refractory mantle heterogeneity will only melt at mantle depths shallower than 20 km in the hottest wedge (T_P 1400 - 1500°C).

Relative strength of the residuum plays a key role in the wedge spatial-temporal patterns of upwelling. Low viscosity heterogeneity interface shallowing with time can produce an age progressive melting track (e.g., Fig. 15b). Rise velocities beneath a weak mantle heterogeneity decrease with distance from the extension axis (Fig. 14c) as wedge fluid is entrained by slab downdip flows. West of the extensional axis, weak heterogeneity (Exp. 27) shallows as it approaches the slab at westward migration rates of ~3 cm min^{-1}, ~2. 4 cm yr^{-1} when scaled to the mantle, creating an age progression in melt generation. As the feature gets closer to the slab, downward entrainment of wedge material decreases upwelling between the trench and ~5 cm (~325 km) from the trench. The low viscosity residuum to the east of the extensional axis experiences a different pattern of interface shallowing. In our analog model there is no strong driver of convection, e.g. the slab, entraining upwelling towards the east. Rise of mantle material and shallowing of residuum interface decreases drastically 21 – 22 cm (~1400 km) from the slab (Fig. 14a). In the long term, as the extension axis migrates westward, further away from the eastern heterogeneity, upwelling velocities beneath the interface will decrease to zero unless an additional source of upwelling is introduced.

Similar to the weak heterogeneity case, predictions on west and east age progression patterns in melting with a strong heterogeneity present in the wedge are linked to residuum-mantle interface rise in P-T space. The high viscosity residuum (Exp. 18) redirects BAE-induced upwelling around the east and west sides (Fig. 14c).

As the extension axis migrates westward at 3 cm min^{-1}, vertical flows preferentially rise up the right side of the feature. Consequently, rising of residuum and ambient fluid is strongest in the east. Weaker upwelling is detected west of the BAE axis, as flow near the trench compete with the downward entrainment of the slab. 1 cm min^{-1} (~0.8 cm yr^{-1} scaled to mantle) westward progression of residuum is occurring to the west of the extensional axis. However, the eastern side is coupled to an overriding plate that has zero horizontal velocity. Upwelling exists to the east of the BAE location but without an additional driver allowing eastward progression of interface in an absolute reference frame, there appears to be no eastward age progression in this wedge. Only in a fixed trench/fixed BAE reference frame does the eastern edge have relative eastward progression.

4.1.3 Effect of Residuum Initial Position

A north-south (trench-parallel) offset is observed in cases where residuum is initially located north of the slab centerline (Exp. 23 and 30). Trench-parallel translation is a consequence of deformation induced by trench rollback (Fig. 16). Both weak and strong residua are initially located north of the slab centerline (Fig. 2c, location 'B'). Weak heterogeneity migrates south at a maximum rate of ~5.5 cm min^{-1}. From 20 Ma to 10 Ma, the residuum's northern most edge has moved ~7 cm to the south, corresponding to ~450 km in the mantle (Fig. 16b). As we saw in previous velocity results, particle trench-parallel velocities decrease towards the slab centerline (e.g., Fig. 13). The southward migration rate of the transported residuum from 10 – 0 Ma lessens and the total trench-parallel offset is 550 km after 20 Ma evolution (Fig. 16c). Similarly to previous cases with BAE, northern wedge residuum morphology experiences trench-normal stretching over 20 Ma due to combined slab and upper plate extensional forcing. At $t^* = 1$, the weak heterogeneity morphology forms a long linear east-west track, extending from the trench to 25 cm (~1625 km) in the east. This feature is extremely thin in the north-south extent (~4 cm, ~260 km). Comparatively, lower north-south migration and less deformation occur when high viscosity heterogeneity is present in the wedge (Fig. 16d – f). Trench-parallel translation rates up to ~3 cm min^{-1} move residuum south by ~7 cm (~450 km) over 20 Ma. The strong residuum remains robust throughout and trench-normal extension is restrained due to the east-west stress guide.

5. Discussion

The experiment results produce general aspects of residuum interaction in 4D circulation and specific results relate to the Cascades system. Fundamental geodynamic modeling results are that: (1) U_T-induced toroidal flow plus U_D-controlled entrainment make distinct regimes of horizontal, or translational, flows away from centerline and vertical velocities in the central wedge. Presence of a residuum that deforms towards the centerline alters rates of horizontal return flow and, perhaps more importantly, vertical flow along the slab centerline. (2) Introduction of a fully coupled mantle surface dramatically changes wedge return flows, thereby impacting long-term mass and energy transport of wedge fluid and residuum. (3) The presence of back-arc extension in the overriding plate provides a striking return flow regime boundary for wedge flow. The extensional axis acts as a barrier to for wedge material. Fluid east of the extensional axis is not readily entrained by the subducting slab. Activated return flows result in increased trench-parallel edge flows west, i.e. trenchward, of the extension location. (4) Interplay between complex 4D flow and thermal-chemical rheological heterogeneity can produce strong indicators in volcanic production at Earth's surface. Slab and BAE induced flow interacting with an evolving residuum can produce linear, time-progressive melting tracks without the use of a deep mantle plume conduit. Relative strength and composition of the residuum play key roles in the timing and composition of the melt.

We can apply the observations we've made in our experiment results to the Cascades. Three distinct models attempt to explain the post-20 Ma thermal evolution

of the Cascadia subduction system. Plume models invoke a thermally buoyant deep mantle upwelling to explain post-20 Ma magmatic events CSFB, HLP and SRP. Typically, plume models attribute the Columbia River/Steens flood basalts to processes related to plume head interaction with the lithosphere [e.g., *Richards et al.*, 1989; *Takahahshi et al.*, 1998; *Camp and Hanan*, 2008; *Wolff et al.*, 2008; *Obrebski et al.*, 2010]. Subsequent eastward trending SRP volcanism is the surface expression for the long-lived conduit tail [e.g., *Pierce and Morgan*, 2009; *Kincaid et al.*, 2013], and the westward trending HLP volcanic track is due to the deformations and entrainment of remaining plume head modified upper mantle [e.g., *Jordan et al.*, 2004; *Kincaid et al.*, 2013]. Non-plume models invoke plate-driven processes, rather than a mantle plume, to control mantle dynamics and volcanism in the Pacific Northwest. Subduction-related processes such as slab steepening, rollback, and extension in the overriding plate lead to a pulse of rapid mantle upwelling responsible for the CSFB event [e.g., *Faccenna et al.*, 2010; *Liu and Stegman*, 2012; *Long et al.*, 2012]. In *Long et al.* [2012] three-dimensional slab rollback-controlled mantle flow along with eroding of the overriding lithosphere explains the westward progressing HLP volcanism but this conceptual model, and other non-plume models, struggle in providing an explanation for the eastward trending magmatism of the SRP.

Our results represent an extension of the *Long et al.* [2012] non-plume model by adding in the effect of residuum produced by a large scale upwelling event at ~20 Ma due to changes in plate mechanics. Experiments begin from this point and show that various parameter choices improve or diminish the match with basic observations. Table 2 summarizes these for geology and seismology. All experiments indicate that

the north-south offset between the CSFB and the HLP/SRP volcanic tracks is the result of slab migration induced toroidal flow. U_D and U_T naturally produce horizontal, melt unfavorable regions over most of the wedge, except along the centerline. Our models constrain mantle upwelling beneath a trench-normal, east-west linear track, thereby placing decompression melting favorable environment beneath the HLP and SRP regions. Residuum that is defined to occupy this region prior to entrainment towards slab and eventual flushing can sharply influence local vertical velocities, i.e. volcanic trends.

Our models that include back-arc extension in the overriding plate are the most successful in linking experiment results with geological observations of the PNW (e.g., Fig. 17). Interaction between wedge upwelling induced by the extension center and a deforming residuum results in time-progressive melting patterns. In the previous section we resolved that westward age-progressive melting west of the BAE axis, i.e., beneath the HLP, is readily explained in cases with strong or weak residuum present. However, there is one preferred model that appears capable of upwelling and possible eastward progressing lavas under SRP. Cases with strong heterogeneity located under an overriding plate with BAE result in the largest upwelling east of the extension location, beneath the SRP region (Fig. 14c). High viscosity residuum that resists deformation tends to alter the natural pattern in upwelling along the slab centerline of this system. The resistance to deformation manifests itself as diverted and focused upwelling along the eastern and western edges of the residuum as depicted in schematic models, i.e., region beneath HLP and SRP [e.g., *Humphreys et al.*, 2000; *Smith et al.*, 2009]. This pattern tends to only occur where residuum is present and so

the progressive accumulation of this material towards the centerline also focuses the trend of east end and west end upwelling along tracks at the centerline. This is consistent with north-south offset of the CSFB and the HLP/SRP and the centered, linear nature of these age-progressive volcanic tracks. While this is the best case for any form of upwelling under the SRP, it does not closely model the eastward age-progressive nature of the rhyolitic lavas. Perhaps if actual melting and hardening of residuum were modeled, as in *Hall and Kincaid* [2004] or *Humphreys et al.* [2000], then eastward progression of upwelling could be achieved. However, this additional model complexity is beyond the scope of this study.

Thus, our results indicate that a third set of models invoking flood basalt residuum interaction with 4D mantle flow can affect mantle dynamics and provide insight into post-20 Ma volcanism of the Pacific Northwest. The fate of chemical and rheological mantle heterogeneity, i.e. residuum, resulting from the CSFB melting event has been explored in both plume [e.g., *Smith et al.*, 2009] and non-plume [e.g., *Humphreys et al.*, 2000] explanations of Cascades melting. Our models show that the deformation of refractory mantle flood basalt residuum created during a massive melting event, such as the ~20 Ma CSFB, can influence upper mantle circulation and surface volcanism over long time scales (at least 80 Ma). Similar to the works of *Humphreys et al.*, 2000, the interface between the refractory residuum and fertile mantle acts as a guide for melting and can result in age-progressive volcanism without a plume conduit. Though our model readily explains the bimodal melting beneath the HLP/SRP tracks and the westward progressing lavas beneath the HLP, the SRP

eastward progressing lavas prove enigmatic and may require additional model features.

Our melt residuum models do not rule out the presence of a deep-seated mantle plume beneath the Pacific Northwest but offer a different explanation for the tectonomagmatism of the last 20 Ma. Similar to *Long et al.* [2012], our models emphasize the importance of 3D subduction-related processes, including rollback and extension, in controlling mantle dynamics and melting. However, the introduction of viscous mantle heterogeneity within the subduction system of our models leads to different results than the conceptual non-plume model of *Long et al.* [2012]. For example, our experimental results do no invoke lithospheric thinning beneath the HLP to produce upwelling related mantle melting. Instead magma production beneath the HLP in our experiments is achieved by flow interaction with an evolving refractory residuum interface. Also, the study of *Long et al.* [2012] cannot explain the SRP-Yellowstone track without the addition of a buoyant mantle upwelling possibly sourced from the uppermost lower mantle. In contrast, our analysis of upwelling patterns in and around the interface of a residuum located beneath a migrating back-arc extension axis shows vertical rise velocities to the east, beneath the Snake River Plain region. But, as we've discussed previously, the eastward age-progression melting is indiscernible in our models.

Our mantle residuum models share similarities with previous Pacific Northwest melting models that invoke a CSFB residuum. *Smith et al.* [2009], *Humphreys et al.* [2000], and our subduction system-residuum models indicate the potential for refractory mantle heterogeneity to deform over time and impact wedge

flows as it evolves. In these models the mantle heterogeneity created during the CSFB event is cited as a guiding factor for the general surface volcanism in the post-20 Ma Cascades. Similar to our model, in *Humphreys et al.* [2000] mantle flow and decompression melting causing magmatism results from local plate motions. However, post-20 Ma Pacific Northwest melting in *Smith et al.* [2009] relies on the existence of a deep-seated plume conduit. There are other dissimilarities between these residuum models that are worth examining. The heterogeneity in *Smith et al.* [2009] is created via a plume source. This model explains the eastward progressing volcanism of the SRP via a long-lived Yellowstone mantle plume interacting with a deforming residuum, while the SRP melting origin remains unresolved in our models. There is an interesting dissimilarity between our models and the model proposed in *Humphreys et al.* [2000]. The mantle residuum in *Humphreys et al.* [2000] grows in volume over time. Decompression melting occurring along the edges of the viscous heterogeneity creates more refractory residuum along the residuum interface. Through time the feature expands trench-normally (to the east and west) and bimodal melting progresses further along the HLP and SRP. Our models also show upwelling related decompression melting along the eastern and western sides of the high viscosity heterogeneity beneath the HLP and SRP tracks. However, in our simplified fluid experiments, which utilize a thermally altered path of glucose syrup as a mantle residuum analog, the heterogeneity is free to deform but is limited to the same volume throughout the course of the experiment. We can theorize that creating new residuum along the edges in our model would also deflect the upwelling further eastward and

westward. This additional model complexity would foreseeably create eastward-progressing melting beneath the SRP track.

6. Conclusions

Plate-driven circulation in the subduction system is 3D and time evolving. Most notably, results highlight the importance of lateral return flow in resupplying the wedge. Adding rheological heterogeneity alters wedge circulation and increases 4D flow complexity. Our models indicate residuum in the subduction system affects local mass and energy transport; i.e. presence of strong heterogeneity decreases shallow wedge velocities resulting in increased velocities of deeper fluid towards subduction. Results have long-term implications for the geochemistry of the wedge and fluxing of mantle to Earth's deep interior. Viscosity variations representing thermal-chemical heterogeneity in the wedge can have residence times much longer than expected, e.g., weak heterogeneity lifetime > 80 Ma in the wedge. The residuum experiments with downdip and rollback slab motion and back-arc extension in the overriding plate have important implications for the Cascades. A north-south offset between Columbia River/Steens Flood Basalts and the High Lava Plains/Snake River Plain tracks are a consequence of deformations induced by trench-rollback. Slab entrainment coupled with back-arc extension trench-normal stretching results in east-west elongated feature beneath High Lava Plain and Snake River Plain. The relative strength and chemical composition of the residuum beneath the extension axis will effect upwelling related decompression melting patterns and compositions**.** The model results in shallow, trench-normal vertical rise of wedge fluid beneath the High Lava Plain and Snake River Plain tracks. However, age progression in melting is complicated. Our results are hard pressed to fit Pacific Northwest observations, especially the enigmatic

eastward melting of the Snake River Plain-Yellowstone track. However, the addition of model complexities, e.g., allowing for residuum volume growth, would produce better-matched laboratory results to the post-20 Ma Cascades geological constraints.

References

Anderson, D. L., and J. H. Natland (2005), A brief history of the plume hypothesis and its competitors: Concept and controversy, in *Special Paper 388: Plates, plumes and paradigms*, vol. 388, pp. 119–145, Geological Society of America.

Armstrong, R. L., W. P. Leeman, and H. E. Malde (1975), K-Ar dating, Quaternary and Neogene volcanic rocks of the Snake River Plain, Idaho, *Am. J. Sci.*, *275*(3), 225–251, doi:10.2475/ajs.275.3.225.

Atwater, T. (1970), Implications of Plate Tectonics for the Cenozoic Tectonic Evolution of Western North America, *Geol. Soc. Am. Bull.*, *81*(12), 3513–3536, doi:10.1130/0016-7606(1970)81[3513:IOPTFT]2.0.CO;2.

Atwater, T., and J. Stock (1998), Pacific-North America Plate Tectonics of the Neogene Southwestern United States: An Update, *Int. Geol. Rev.*, *40*(5), 375–402, doi:10.1080/00206819809465216.

Camp, V. E., and B. B. Hanan (2008), A plume-triggered delamination origin for the Columbia River Basalt Group, *Geosphere*, *4*(3), 480–495, doi:10.1130/GES00175.1.

Camp, V. E., and M. E. Ross (2004), Mantle dynamics and genesis of mafic magmatism in the intermontane Pacific Northwest, *J. Geophys. Res. Solid Earth*, *109*(B8), B08204, doi:10.1029/2003JB002838.

Carlson, R. W. (1984), Isotopic constraints on Columbia River flood basalt genesis and the nature of the subcontinental mantle, *Geochim. Cosmochim. Acta*, *48*(11), 2357–2372, doi:10.1016/0016-7037(84)90231-X.

Carlson, R. W., and W. K. Hart (1987), Crustal genesis on the Oregon Plateau, *J. Geophys. Res. Solid Earth*, *92*(B7), 6191–6206, doi:10.1029/JB092iB07p06191.

Christiansen, R. L., and E. H. McKee (1978), 13: Late Cenozoic volcanic and tectonic evolution of the Great Basin and Columbia Intermontane regions, *Geol. Soc. Am. Mem.*, *152*, 283–312, doi:10.1130/MEM152-p283.

Christiansen, R. L., G. R. Foulger, and J. R. Evans (2002), Upper-mantle origin of the Yellowstone hotspot, *Geol. Soc. Am. Bull.*, *114*(10), 1245–1256, doi:10.1130/0016-7606(2002)114<1245:UMOOTY>2.0.CO;2.

Crisp, J. A. (1984), Rates of magma emplacement and volcanic output, *J. Volcanol. Geotherm. Res.*, *20*, 177–211, doi:10.1016/0377-0273(84)90039-8.

Cross, T. A., and R. H. Pilger (1978), Constraints on absolute motion and plate interaction inferred from Cenozoic igneous activity in the western United States, *Am. J. Sci.*, *278*(7), 865–902, doi:10.2475/ajs.278.7.865.

Draper, D. S. (1991), Late cenozoic bimodal magmatism in the northern basin and range province of southeastern Oregon, *J. Volcanol. Geotherm. Res.*, *47*(3–4), 299–328, doi:10.1016/0377-0273(91)90006-L.

Druken, K. A., M. D. Long, and C. Kincaid (2011), Patterns in seismic anisotropy driven by rollback subduction beneath the High Lava Plains, *Geophys. Res. Lett.*, *38*(13), L13310, doi:10.1029/2011GL047541.

Eaton, G. P. (1984), The miocene Great Basin of Western North America as an extending back-arc region, *Tectonophysics*, *102*(1–4), 275–295, doi:10.1016/0040-1951(84)90017-9.

Ellis, B. S., J. A. Wolff, S. Boroughs, D. F. Mark, W. A. Starkel, and B. Bonnichsen (2013), Rhyolitic volcanism of the central Snake River Plain: a review, *Bull. Volcanol.*, *75*(8), 1–19, doi:10.1007/s00445-013-0745-y.

Faccenna, C., T. W. Becker, S. Lallemand, Y. Lagabrielle, F. Funiciello, and C. Piromallo (2010), Subduction-triggered magmatic pulses: A new class of plumes?, *Earth Planet. Sci. Lett.*, *299*(1–2), 54–68, doi:10.1016/j.epsl.2010.08.012.

Ford, M. T., A. L. Grunder, and R. A. Duncan (2013), Bimodal volcanism of the High Lava Plains and Northwestern Basin and Range of Oregon: Distribution and tectonic implications of age-progressive rhyolites, *Geochem. Geophys. Geosystems*, *14*(8), 2836–2857, doi:10.1002/ggge.20175.

Foulger, G. R. (2003), Do plumes exist? Discussing the origin of "hotspot" volcanism, *www.MantlePlumes.org*. Available from: www.mantleplumes.org

Foulger, G. R. (2005), Mantle plumes: Why the current skepticism, *Chin. Sci. Bull.*, *50*(15), 1555–1560, doi:10.1360/982005-919.

Foulger, G. R., J. H. Natland, D. C. Presnall, Geophysical Laboratory, and D. L. Anderson (Eds.) (2005), *Plates, Plumes, And Paradigms*, Geological Society of Amer, Boulder, Colo.

Funiciello, F., C. Faccenna, D. Giardini, and K. Regenauer-Lieb (2003), Dynamics of retreating slabs: 2. Insights from three-dimensional laboratory experiments, *J. Geophys. Res. Solid Earth*, *108*(B4), 2207, doi:10.1029/2001JB000896.

Funiciello, F., M. Moroni, C. Piromallo, C. Faccenna, A. Cenedese, and H. A. Bui (2006), Mapping mantle flow during retreating subduction: Laboratory models analyzed by feature tracking, *J. Geophys. Res. Solid Earth*, *111*(B3), B03402, doi:10.1029/2005JB003792.

Geist, D., and M. Richards (1993), Origin of the Columbia Plateau and Snake River plain: Deflection of the Yellowstone plume, *Geology*, *21*(9), 789–792, doi:10.1130/0091-7613(1993)021<0789:OOTCPA>2.3.CO;2.

Griffiths, R. W., R. I. Hackney, and R. D. van der Hilst (1995), A laboratory investigation of effects of trench migration on the descent of subducted slabs, *Earth Planet. Sci. Lett.*, *133*(1–2), 1–17, doi:10.1016/0012-821X(95)00027-A.

Hall, P. S., and C. Kincaid (2001), Diapiric Flow at Subduction Zones: A Recipe for Rapid Transport, *Science*, *292*(5526), 2472–2475, doi:10.1126/science.1060488.

Hall, P. S., and C. Kincaid (2004), Melting, dehydration, and the geochemistry of off-axis plume-ridge interaction, *Geochem. Geophys. Geosystems*, *5*(12), Q12E18, doi:10.1029/2003GC000667.

Hirschmann, M. M. (2010), Partial melt in the oceanic low velocity zone, *Phys. Earth Planet. Inter.*, *179*(1–2), 60–71, doi:10.1016/j.pepi.2009.12.003.

Hirth, G., and D. Kohlstedt (2003), Rheology of the upper mantle and the mantle wedge: A view from the experimentalists, in *Inside the Subduction Factory*, vol. 138, edited by J. Eiler, pp. 83–105, Geophysical Monography American Geophysical Union, Washington, D.C.

Hooper, P. R., V. E. Camp, S. P. Reidel, and M. E. Ross (2007), The origin of the Columbia River flood basalt province: Plume versus nonplume models, *Geol. Soc. Am. Spec. Pap.*, *430*, 635–668, doi:10.1130/2007.2430(30).

Humphreys, E. D., and D. D. Coblentz (2007), North American dynamics and western U.S. tectonics, *Rev. Geophys.*, *45*(3), RG3001, doi:10.1029/2005RG000181.

Humphreys, E. D., K. G. Dueker, D. L. Schutt, and R. B. Smith (2000), Beneath Yellowstone; evaluating plume and nonplume models using teleseismic images of the upper mantle, *GSA Today*, *10*(12), 1–7.

Jadamec, M. A., and M. I. Billen (2012), The role of rheology and slab shape on rapid mantle flow: Three-dimensional numerical models of the Alaska slab edge, *J. Geophys. Res. Solid Earth*, *117*(B2), B02304, doi:10.1029/2011JB008563.

James, D. E., M. J. Fouch, J. C. VanDecar, and S. van der Lee (2001), Tectospheric structure beneath southern Africa, *Geophys. Res. Lett.*, *28*(13), 2485–2488, doi:10.1029/2000GL012578.

Jordan, B. T. (2005), Age-progressive volcanism of the Oregon High Lava Plains: Overview and evaluation of tectonic models, *Geol. Soc. Am. Spec. Pap.*, *388*, 503–515, doi:10.1130/0-8137-2388-4.503.

Jordan, B. T., A. L. Grunder, R. A. Duncan, and A. L. Deino (2004), Geochronology of age-progressive volcanism of the Oregon High Lava Plains: Implications for the plume interpretation of Yellowstone, *J. Geophys. Res. Solid Earth*, *109*(B10), B10202, doi:10.1029/2003JB002776.

Jordan, T. H. (1975), The continental tectosphere, *Rev. Geophys.*, *13*(3), 1–12, doi:10.1029/RG013i003p00001.

Jordan, T. H. (1978), Composition and development of the continental tectosphere, *Nature*, *274*(5671), 544–548, doi:10.1038/274544a0.

Kincaid, C., and R. W. Griffiths (2004), Variability in flow and temperatures within mantle subduction zones, *Geochem. Geophys. Geosystems*, *5*(6), Q06002, doi:10.1029/2003GC000666.

Kincaid, C., and P. Olson (1987), An experimental study of subduction and slab migration, *J. Geophys. Res. Solid Earth*, *92*(B13), 13832–13840, doi:10.1029/JB092iB13p13832.

Kincaid, C., K. A. Druken, R. W. Griffiths, and D. R. Stegman (2013), Bifurcation of the Yellowstone plume driven by subduction-induced mantle flow, *Nat. Geosci.*, *6*(5), 395–399, doi:10.1038/ngeo1774.

Leeman, W. P. (1982), Development of the Snake River Plain – Yellowstone Plateau province, Idaho and Wyoming: an overview and petrologic model, in *Cenozoic Geology of Idaho: Idaho Bureau of Mines and Geology Bulletin*, vol. 26, edited by B. BONNICHSEN and R. M. BRECKENRIDGE, pp. 155 – 177, Idaho Geological Survey.

Liu, L., and D. R. Stegman (2012), Origin of Columbia River flood basalt controlled by propagating rupture of the Farallon slab, *Nature*, *482*(7385), 386–389, doi:10.1038/nature10749.

Long, M. D., and P. G. Silver (2009), Mantle flow in subduction systems: The subslab flow field and implications for mantle dynamics, *J. Geophys. Res. Solid Earth*, *114*(B10), B10312, doi:10.1029/2008JB006200.

Long, M. D., C. B. Till, K. A. Druken, R. W. Carlson, L. S. Wagner, M. J. Fouch, D. E. James, T. L. Grove, N. Schmerr, and C. Kincaid (2012), Mantle dynamics beneath the Pacific Northwest and the generation of voluminous back-arc volcanism: MANTLE DYNAMICS BENEATH THE PNW, *Geochem. Geophys. Geosystems*, *13*(8), n/a–n/a, doi:10.1029/2012GC004189.

Maaløe, S. (2004), The solidus of harzburgite to 3 GPa pressure: the compositions of primary abyssal tholeiite, *Mineral. Petrol.*, *81*(1-2), 1–17, doi:10.1007/s00710-004-0028-6.

MacDougall, J. G., C. Kincaid, S. Szwaja, and K. M. Fischer (2014), The impact of slab dip variations, gaps and rollback on mantle wedge flow: insights from fluids experiments, *Geophys. J. Int.*, ggu053, doi:10.1093/gji/ggu053.

MacLeod, N. S., G. W. Walker, and E. H. McKee (1975), *Geothermal significance of eastward increase in age of upper Cenozoic rhyolitic domes in southeastern Oregon*, Open-File Report, USGS Numbered Series, U.S. Geological Survey.

Malde, H. E. (1991), Quaternary geology and structural history of the Snake River Plain, Idaho and Oregon, in *Quaternary Nonglacial Geology, Conterminous U.S.: Geology of North America*, vol. K-2, edited by R. B. Morrison, pp. 251 – 281, Geological Society of America, Boulder, CO.

Meigs, A. et al. (2009), Geological and geophysical perspectives on the magmatic and tectonic development, High Lava Plains and northwest Basin and Range, *Field Guid.*, *15*, 435–470, doi:10.1130/2009.fld015(21).

Morgan, W. J. (1972), Plate Motions and Deep Mantle Convection, *Geol. Soc. Am. Mem.*, *132*, 7–22, doi:10.1130/MEM132-p7.

Obrebski, M., R. M. Allen, M. Xue, and S.-H. Hung (2010), Slab-plume interaction beneath the Pacific Northwest, *Geophys. Res. Lett.*, *37*(14), L14305, doi:10.1029/2010GL043489.

Olson, P. (1990), Hot spots, swells and mantle plumes, in *Magma Transport and Storage*, edited by M. P. Ryan, pp. 33 – 50, John Wiley & Sons Ltd.

Olson, P., and C. Kincaid (1991), Experiments on the interaction of thermal convection and compositional layering at the base of the mantle, *J. Geophys. Res.*, *96*(B3), 4347, doi:10.1029/90JB02530.

Pierce, K. L., and L. A. Morgan (2009), Is the track of the Yellowstone hotspot driven by a deep mantle plume? — Review of volcanism, faulting, and uplift in light of new data, *J. Volcanol. Geotherm. Res.*, *188*(1–3), 1–25, doi:10.1016/j.jvolgeores.2009.07.009.

Pierce, K. L., L. A. Morgan, and R. W. Saltus (2000), *Yellowstone plume head, postulated tectonic relations to the Vancouver Slab, continental boundaries, and climate: USGS Open-File Report 2000-498*, BiblioGov.

Pollack, H. N. (1986), Cratonization and thermal evolution of the mantle, *Earth Planet. Sci. Lett.*, *80*(1-2), 175–182, doi:10.1016/0012-821X(86)90031-2.

Richards, M. A., R. A. Duncan, and V. E. Courtillot (1989), Flood Basalts and Hot-Spot Tracks: Plume Heads and Tails, *Science*, *246*(4926), 103–107, doi:10.1126/science.246.4926.103.

Schellart, W. P. (2004), Kinematics of subduction and subduction-induced flow in the upper mantle, *J. Geophys. Res. Solid Earth*, *109*(B7), B07401, doi:10.1029/2004JB002970.

Schutt, D. L., and K. Dueker (2008), Temperature of the plume layer beneath the Yellowstone hotspot, *Geology*, *36*(8), 623–626, doi:10.1130/G24809A.1.

Schutt, D. L., and E. D. Humphreys (2004), P and S wave velocity and VP/VS in the wake of the Yellowstone hot spot, *J. Geophys. Res. Solid Earth*, *109*(B1), B01305, doi:10.1029/2003JB002442.

Schutt, D. L., K. Dueker, and H. Yuan (2008), Crust and upper mantle velocity structure of the Yellowstone hot spot and surroundings, *J. Geophys. Res. Solid Earth*, *113*(B3), B03310, doi:10.1029/2007JB005109.

Smith, R. B., M. Jordan, B. Steinberger, C. M. Puskas, J. Farrell, G. P. Waite, S. Husen, W.L. Chang, and R. O'Connell (2009), Geodynamics of the Yellowstone hotspot and mantle plume: Seismic and GPS imaging, kinematics, and mantle flow, *J. Volcanol. Geotherm. Res.*, *188*(1–3), 26–56, doi:10.1016/j.jvolgeores.2009.08.020.

Swanson, D. A., T. L. Wright, P. R. Hooper, and R. D. Bentley (1979), *Revisions in stratigraphic nomenclature of the Columbia River Basalt Group*, United States Geological Survey.

Takahahshi, E., K. Nakajima, and T. L. Wright (1998), Origin of the Columbia River basalts: melting model of a heterogeneous plume head, *Earth Planet. Sci. Lett.*, *162*(1–4), 63–80, doi:10.1016/S0012-821X(98)00157-5.

Thompson, R. N., and S. A. Gibson (2000), Transient high temperatures in mantle plume heads inferred from magnesian olivines in Phanerozoic picrites, *Nature*, *407*(6803), 502–506, doi:10.1038/35035058.

Tolan, T. L., S. P. Reidel, M. H. Beeson, J. L. Anderson, K. R. Fecht, and D. A. Swanson (1989), Revisions to the estimates of the areal extent and volume of the Columbia River Basalt Group, *Geol. Soc. Am. Spec. Pap.*, *239*, 1–20, doi:10.1130/SPE239-p1.

Toomey, D. R., W. S. D. Wilcock, S. C. Solomon, W. C. Hammond, and J. A. Orcutt (1998), Mantle Seismic Structure Beneath the MELT Region of the East Pacific Rise from P and S Wave Tomography, *Science*, *280*(5367), 1224–1227, doi:10.1126/science.280.5367.1224.

Villagómez, D. R., D. R. Toomey, D. J. Geist, E. E. E. Hooft, and S. C. Solomon (2014), Mantle flow and multistage melting beneath the Galapagos hotspot revealed by seismic imaging, *Nat. Geosci.*, *7*(2), 151–156, doi:10.1038/ngeo2062.

Wagner, L. S., M. J. Fouch, D. E. James, and S. Hanson-Hedgecock (2012), Crust and upper mantle structure beneath the Pacific Northwest from joint inversions of ambient noise and earthquake data, *Geochem. Geophys. Geosystems*, *13*(12), Q0AN03, doi:10.1029/2012GC004353.

Waite, G. P., D. L. Schutt, and R. B. Smith (2005), Models of lithosphere and asthenosphere anisotropic structure of the Yellowstone hot spot from shear wave splitting, *J. Geophys. Res. Solid Earth*, *110*(B11), B11304, doi:10.1029/2004JB003501.

Waite, G. P., R. B. Smith, and R. M. Allen (2006), VP and VS structure of the Yellowstone hot spot from teleseismic tomography: Evidence for an upper mantle plume, *J. Geophys. Res. Solid Earth*, *111*(B4), B04303, doi:10.1029/2005JB003867.

Walker, G. P. L. (1993), Basaltic-volcano systems, *Geol. Soc. Lond. Spec. Publ.*, *76*(1), 3–38, doi:10.1144/GSL.SP.1993.076.01.01.

Waters, A. C. (1961), Stratigraphic and lithologic variations in the Columbia River basalt, *Am. J. Sci.*, *259*(8), 583–611, doi:10.2475/ajs.259.8.583.

Wells, R. E., and P. L. Heller (1988), The relative contribution of accretion, shear, and extension to Cenozoic tectonic rotation in the Pacific Northwest, *Geol. Soc. Am. Bull.*, *100*(3), 325–338, doi:10.1130/0016-7606(1988)100<0325:TRCOAS>2.3.CO;2.

Wernicke, B., G. J. Axen, and J. K. Snow (1988), Basin and Range extensional tectonics at the latitude of Las Vegas, Nevada, *Geol. Soc. Am. Bull.*, *100*, 1738 – 1757, doi:10.1130/ 0016-7606(1988)100<1738:BARETA>2.3.CO;2.

White, J., S. Bryan, P.-S. Ross, S. Self, and T. Thordarson (2009), Physical volcanology of continental large igneous provinces: update and review, in *Studies in Volcanology: The Legacy of George Walker*, edited by T. Thordarson, S. Self, G. Larsen, S. Rowland, and A. Hoskuldsson, pp. 291–321, The Geological Society Publishing House, United Kingdom.

Wolff, J. A., F. C. Ramos, G. L. Hart, J. D. Patterson, and A. D. Brandon (2008), Columbia River flood basalts from a centralized crustal magmatic system, *Nat. Geosci.*, *1*(3), 177–180, doi:10.1038/ngeo124.

TABLES

Table 1
Experimental parameters for plate forcings and residuum.

Exp	Slab			Wedge			Residuum				
	U_D (cm/min)	U_T (cm/min)	θ (°)	OP	T_M (°C)	μ_M (Pa s)	x_i (cm)	y_i (cm)	T_R (°C)	μ_R (Pa s)	μ^*
Varied residuum viscosity:											
2	8	3	50		22	134	14	0	22	134	1
5	8	3	50		22	134	14	0	9	1070	8
6	8	3	50		22	134	14	0	32	36	0.3
13	8	3	50		19	207	14	0	33	32	0.1
14	8	3	50		19	207	14	0	13	534	3
Varied slab parameters:											
1a	8	0	50		22	134	14	0	33	32	0.2
1b	8	0	50		22	134	14	0	14	453	3
Varied overriding plate parameters:											
3	8	3	50	OP	20	178	14	0	20	178	1
12	8	3	50	OP	19	207	14	0	53	4	0.02
15	8	3	50	OP	19	207	14	0	7	1546	8
18	8	3	50	BAE	21	154	14	0	7	1546	10
26	8	3	50	BAE	21	154	14	0	21	154	1
27	8	3	50	BAE	21	154	14	0	52	5	0.03
Varied residuum location (Cascades cases):											
23	8	3	50	BAE	21	154	14	6	6	1869	12
30	8	3	50	BAE	20	178	14	6	49	6	0.03

Columns 2–3 represent the average plate forcing conditions for each experiment with U_D and U_T representing the downdip (or longitudinal) sinking and translational rollback speeds of the slab. In the lab, 1 cm min^{-1} is approximately equivalent to 0.8 cm yr^{-1} in the mantle. Dip angle (θ) is given in degrees from horizontal. Columns 4–6 list the wedge parameters, which include the mantle surface conditions for each experiment (OP: with overriding plate, BAE: with back-arc extension, and blank: free slip mantle surface conditions), mantle wedge fluid temperature (T_M) and corresponding viscosity (μ_M). Columns 7–8 list the initial central residuum location (x_i; y_i) where x_i is the distance from the trench and y_i is the distance from the slab centerline. For the majority of experiments the residuum is initially located in the center of the wedge ($x_i = 14$; $y_i = 0$), except for the Cascades cases where the residuum location represents the northern wedge location of the CSFB ($x_i = 13$; $y_i = 6$). Residuum material temperature (T_R) and corresponding viscosity (μ_R) are shown in Columns 9–10. Column 11 lists the residuum-wedge viscosity ratio μ_R/μ_M (μ^*) for each experiment ($\mu^* < 1$: weak mantle heterogeneity present in the mantle wedge, $\mu^* > 1$: strong mantle heterogeneity present, and $\mu^* = 1$: reference cases, no heterogeneity present).

Table 2
Comparison of constraints with models

	Decoupled mantle surface		Coupled mantle surface (OP)		Back-arc extension (BAE)	
	Weak residuum ($\mu^* < 1$)	Strong residuum ($\mu^* > 1$)	Weak residuum ($\mu^* < 1$)	Strong residuum ($\mu^* > 1$)	Weak residuum ($\mu^* < 1$)	Strong residuum ($\mu^* > 1$)
CSFB						
N-S offset: 10 – 15 Ma	✓	✓	×	×	✓	✓
High Lava Plains						
Westward progression	✓	✓	✓	✓	✓	✓
Narrow N-S, wide E-W melting	×	×	×	×	✓	✓
Snake River Plain-Yellowstone						
Eastward progression	×	×	×	×	✓-	✓-
Narrow N-S, wide E-W melting	×	×	×	×	✓	✓

✓: Good agreement, ×: No agreement, ✓-: Agreement with caveats

FIGURES

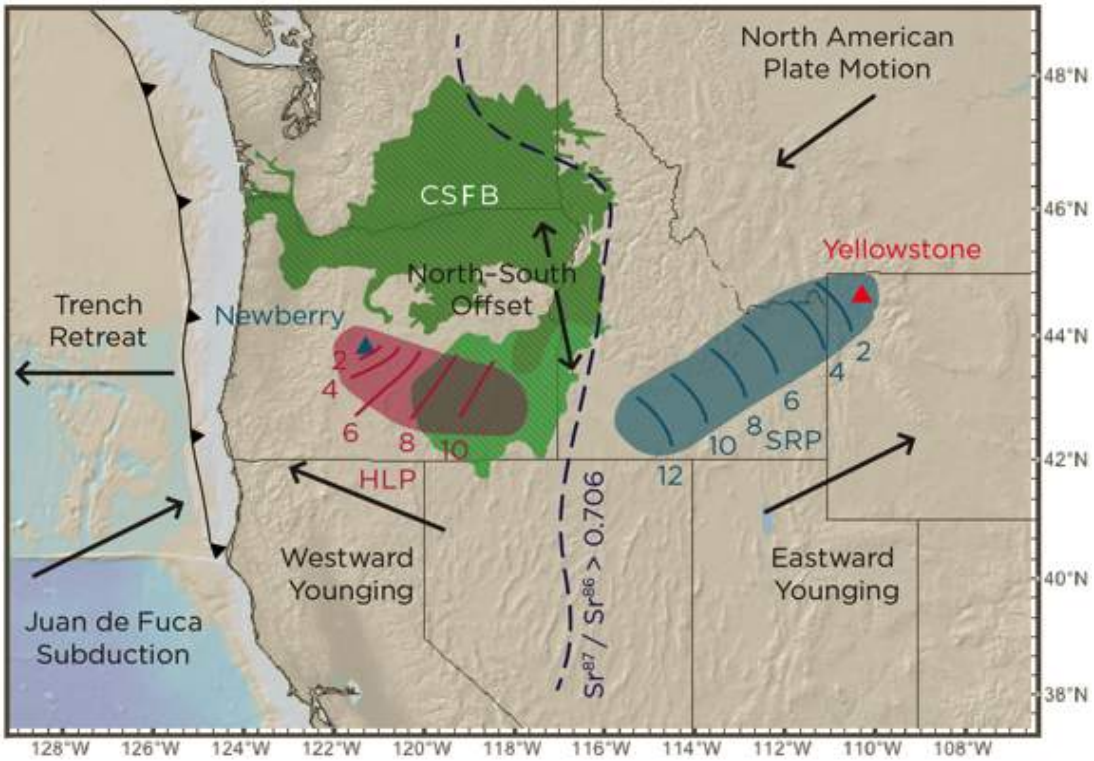

Figure 1. Geologic map of the Pacific-Northwest U.S. showing the Cascades subduction system with key volcanic features: Large igneous province Columbia River/Steens flood basalts (CSFB), shown in green, and southern volcanic tracks High Lava Plains (HLP) and Snake River Plain (SRP) are marked in pink and blue, respectively, and show opposite age progression of rhyolitic lavas in millions of years.

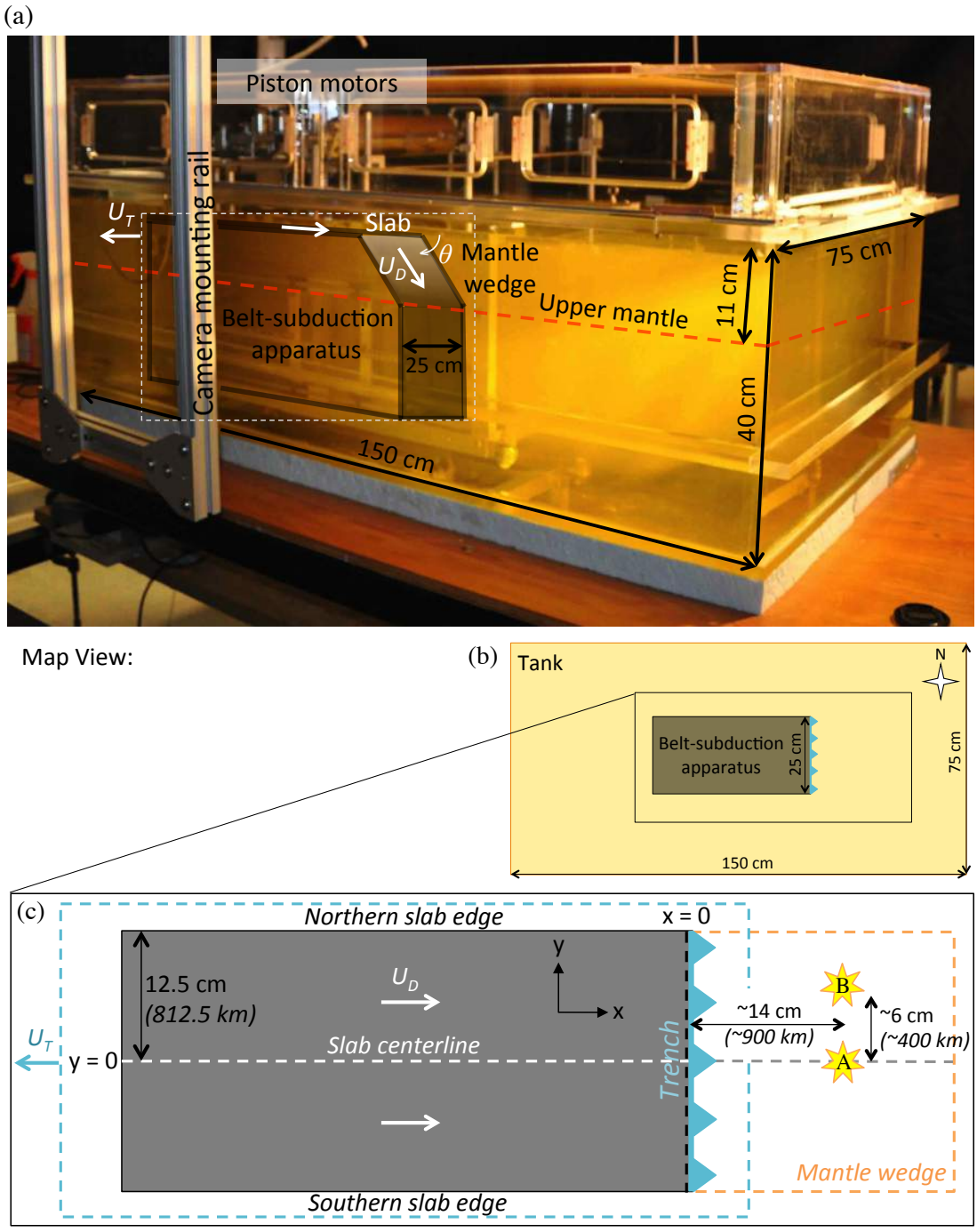

Figure 2. (a) Photograph of the subduction apparatus with the tank of glucose syrup and the reinforced belt system representing subducting plate. White arrows indicate down-dip (U_D) and translational (U_T) slab motions controlled by piston motors located above fluid surface. (b) Scaled map-view cartoon of the lab apparatus. (c) Enlarged inset showing approximate center location of residuum at experiment initiation (yellow stars). In most cases, residuum location is on the slab centerline (star A). In the Cascadia cases (Table 1), residuum initial location is north of the slab centerline (star B).

(a) With overriding plate

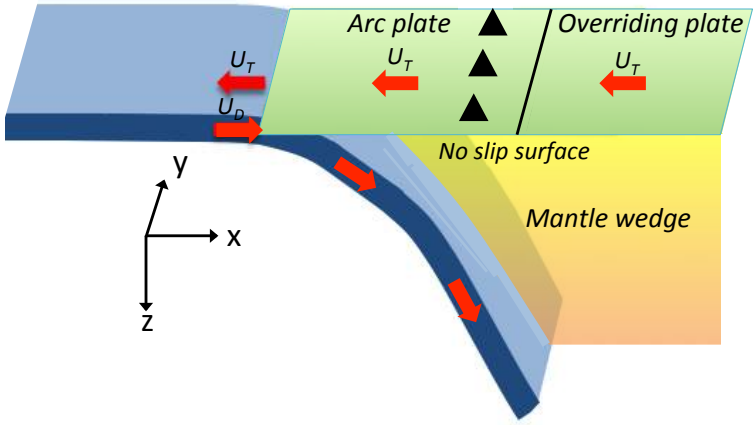

(b) With back-arc spreading center

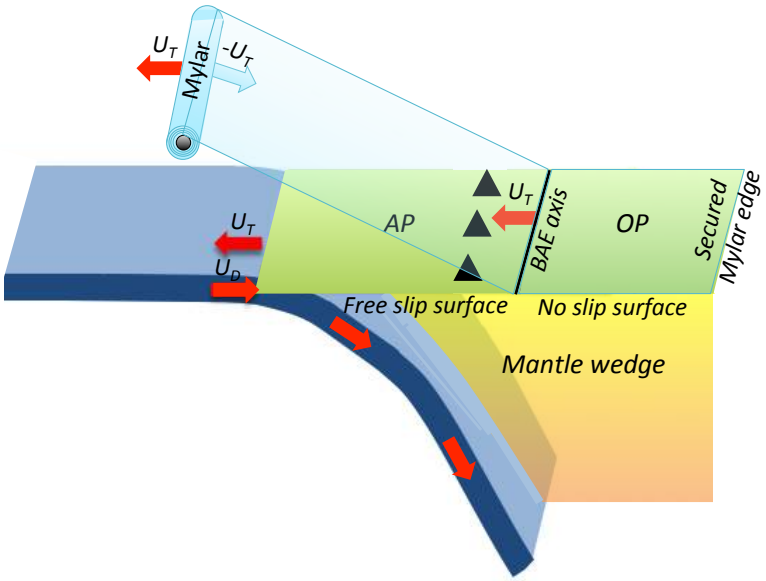

Figure 3. Cartoon schematics illustrating model overriding plates and surface conditions. (a) OP and subducting slab migrate with trench motion. (b) The back-arc extension (BAE) axis moves with trench motion. Mylar spools out from the roller at ($-U_T$). Arrows indicate absolute motion of slab, trench, and extension axis. The OP has zero horizontal velocity and imposes a no slip surface condition on the mantle. The AP have free slip mantle surface.

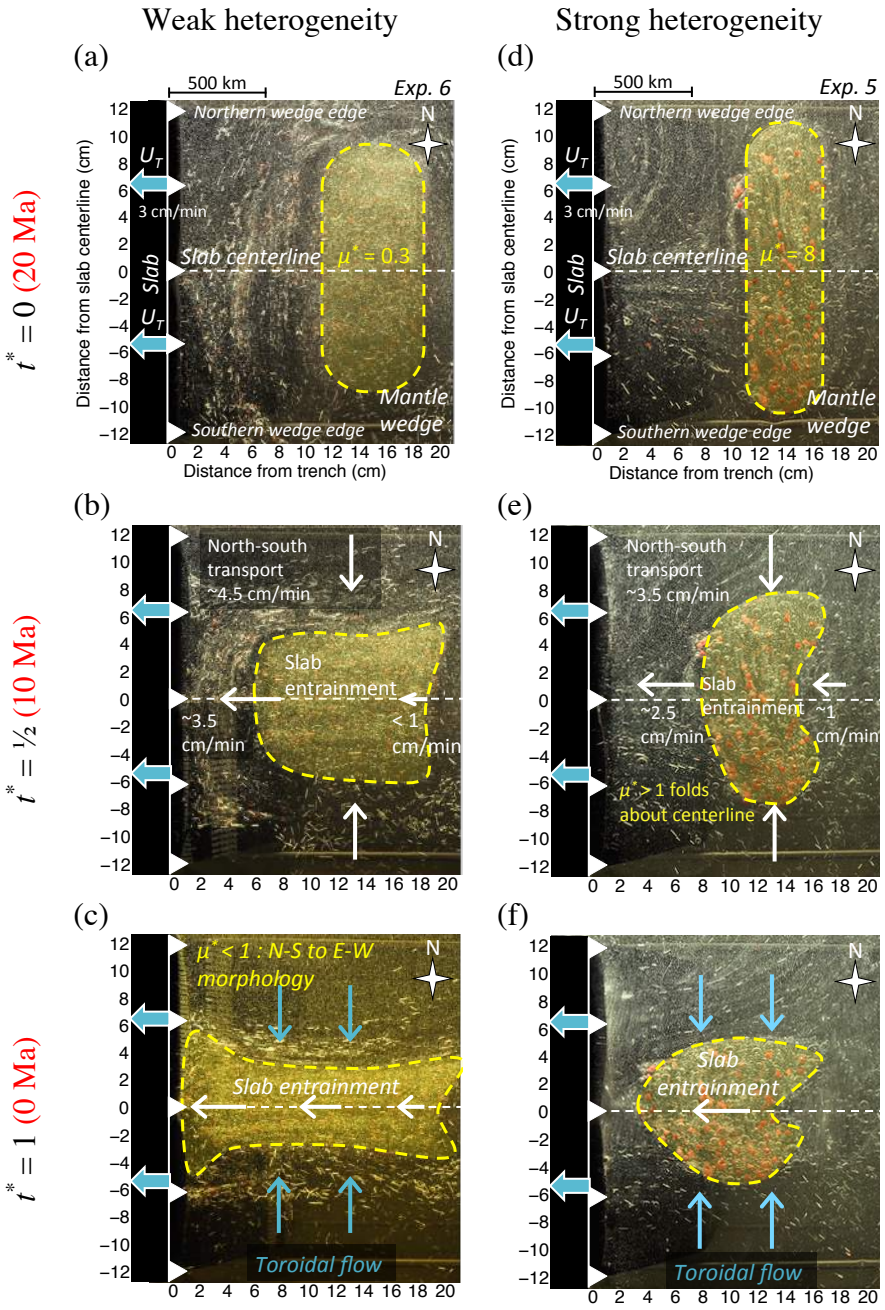

Figure 4. Comparison of map view, 20 Ma evolution of weak (a – c) and strong (d – f) residuum in subduction driven flows with U_T = 3 cm/min and U_D = 8 cm/min. Images show results at depth z = 1 – 2 cm (~ 65 – 130 km) beneath a free slip mantle surface. Residuum structure is highlighted in yellow. Downdip subduction entrains residuum material towards the trench while U_T-induced toroidal flow compresses the residuum towards the slab centerline. $\mu^* < 1$ experiences very efficient pure shear in transition from an initial north-south morphology to an east-west morphology. $\mu^* > 1$ resists internal deformation and folds along the trench-normal symmetry line.

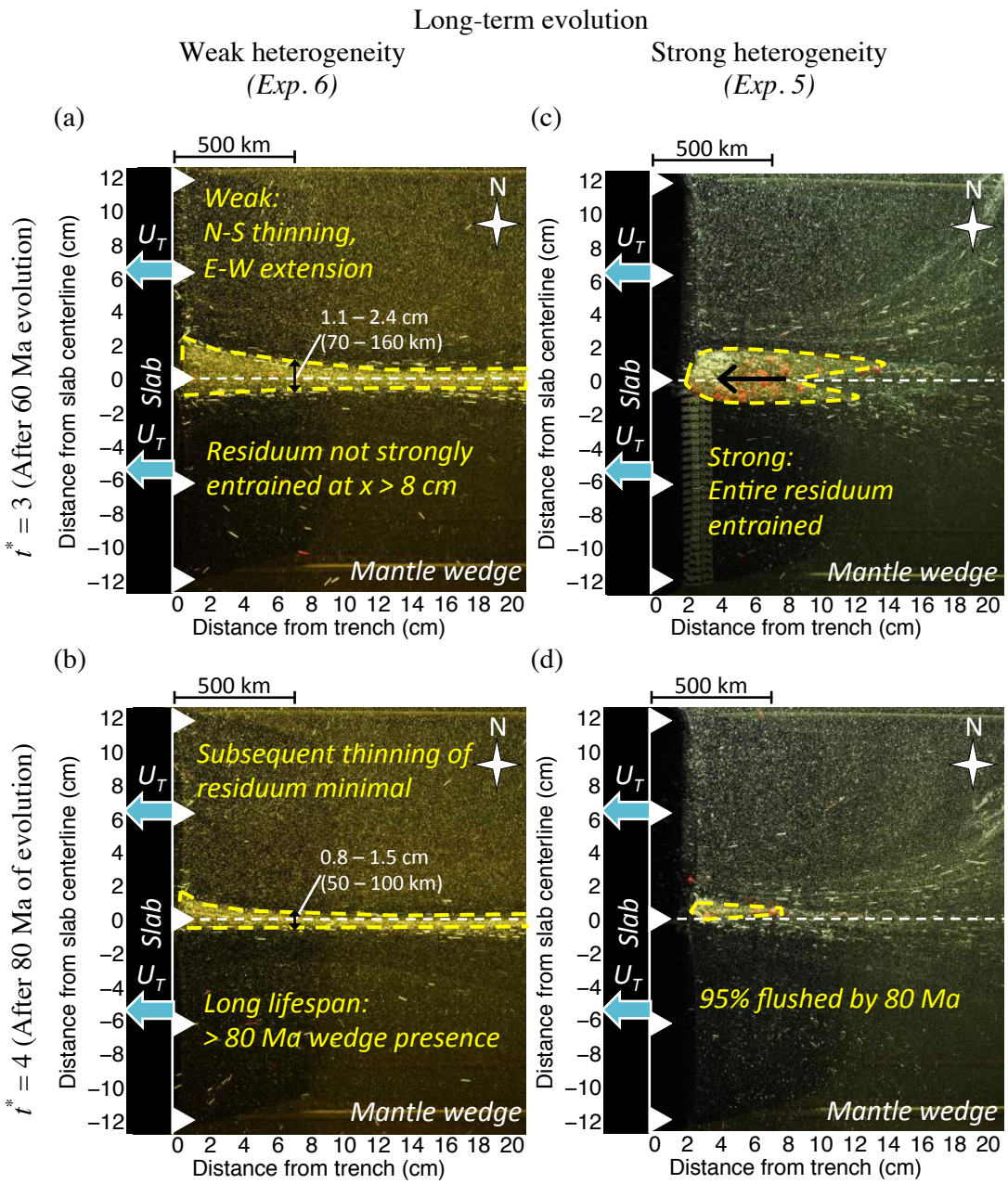

Figure 5. Late stage map view images of (a) – (b) weak residuum (Exp. 6) and (c) – (d) strong residuum (Exp. 5). Top row shows residuum-wedge after 60 My (7.5 minutes in the lab) and bottom row shows wedge results after 80 My (10 minutes in the lab).

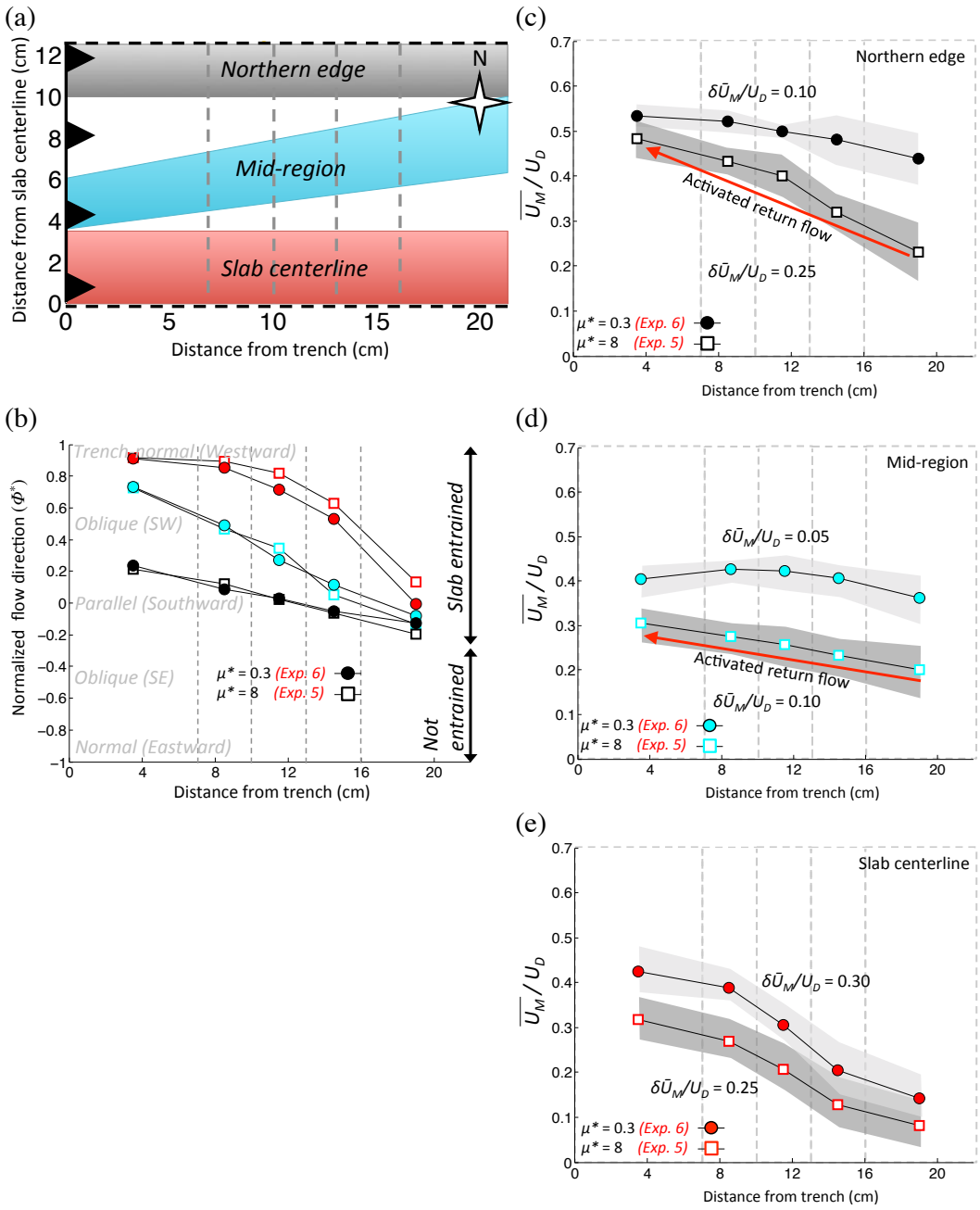

Figure 6. (a) Wedge region divided into three analysis zones: Northern edge (black), mid-region (blue), and slab centerline (red). Grey dashes indicate averaging domains. (b) Average normalized flow direction (Φ^*) and (c – e) average instantaneous flow velocity (U_M/U_D) for case with weak (circles) and strong (squares) residuum. Velocities and direction are averaged from instantaneous flows in $t^* = 0, 0.5$, and 1. Grey shading indicates standard deviation in each averaging domain. $\delta U_M/U_D$ represents change in region average velocity between averaging domains located farthest and nearest to the trench.

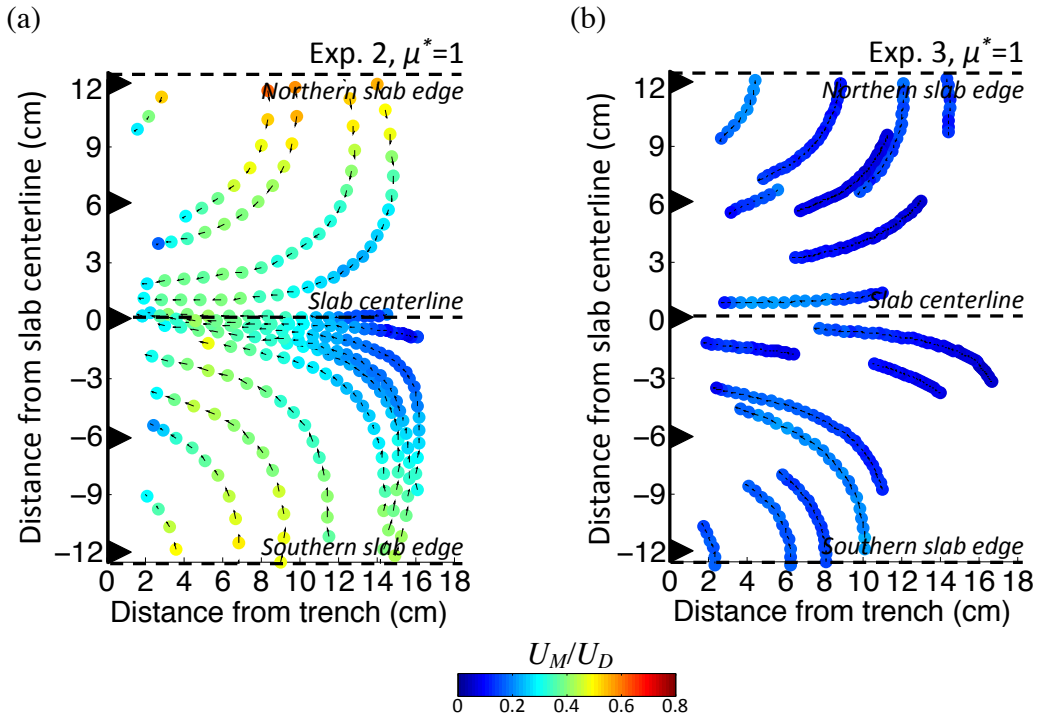

Figure 7. Lagrangian particle velocity for ambient wedge with (a) free slip and (b) no slip surface conditions. Results are in the x-y plane at z = 1 – 2 cm (65 – 130 km). All velocities are calculated in a fixed trench reference frame.

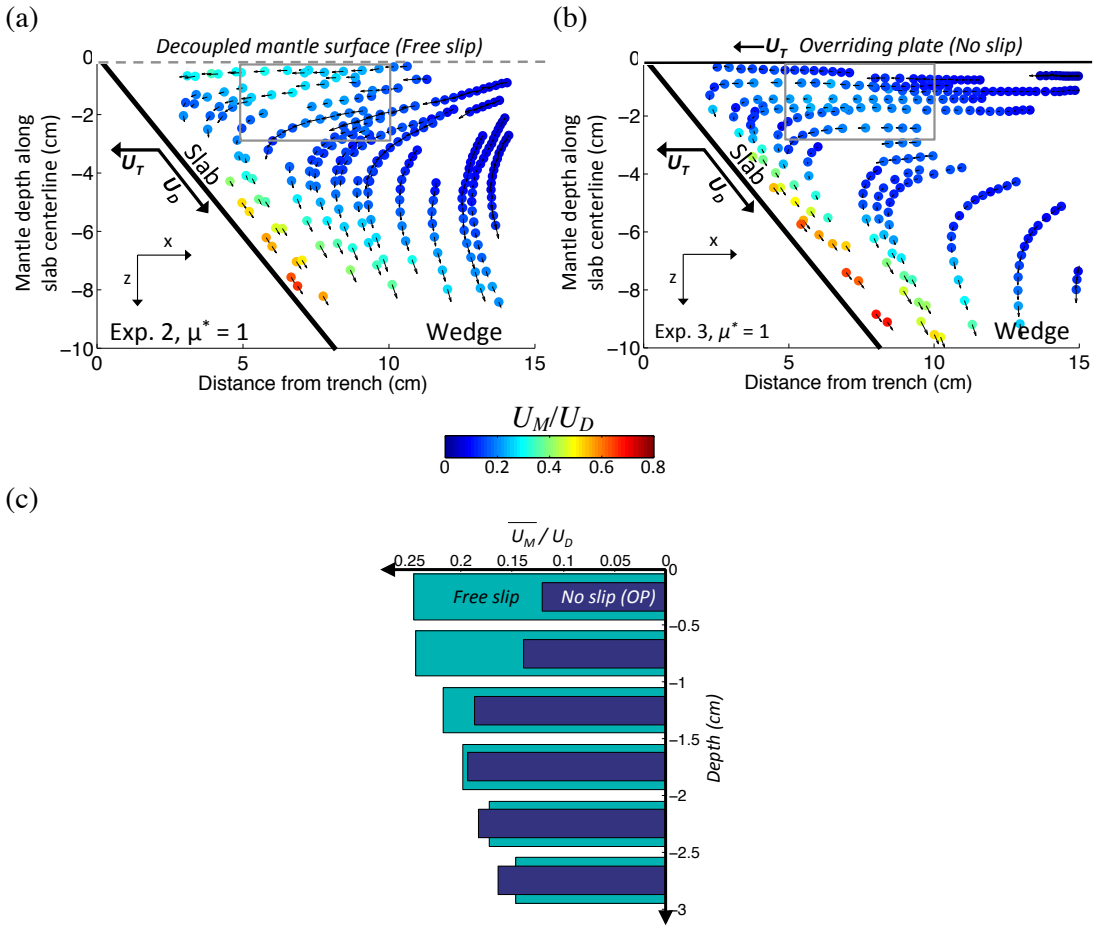

Figure 8. (a) and (b) Identical to Fig. 7, except results are in the x-z plane, along the slab centerline from mantle surface to depth. (c) Average surface flow velocity vs. mantle depth from the shallow mantle domain shown in grey box from (a) and (b).

(a)

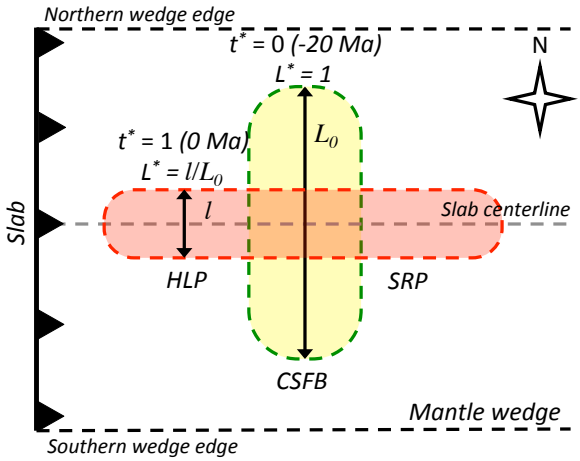

(b)

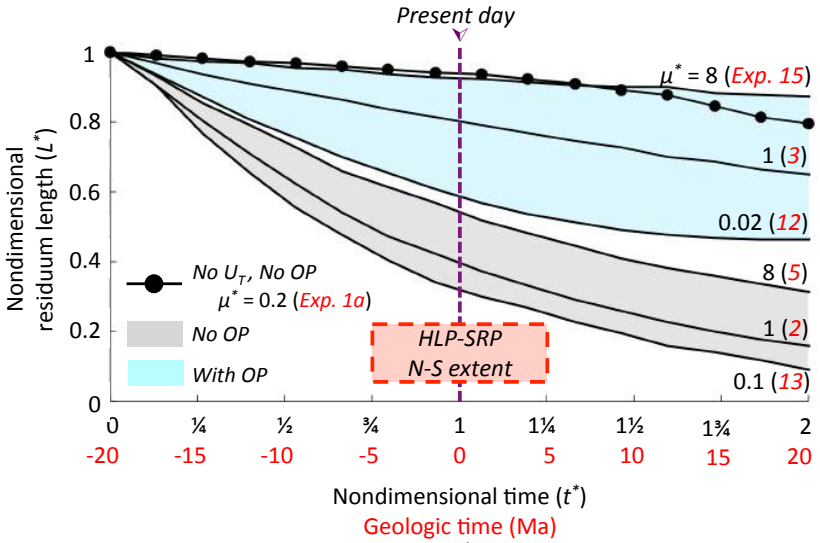

Figure 9. (a) Cartoon illustrating calculation of L^*. Experiment initial residuum length (L_0) is ~20 cm (1300 km). (b) Residuum north-south nondimensionalized length (L^*) over time. Except for Exp. 1a, where $U_T = 0$, all experiments are run with slab rates U_T = 3 cm min^{-1}, U_D = 8 cm min^{-1}. Toroidal flow induced by a migrating trench (U_T) is the major driver of deformation of the mantle wedge heterogeneity. In cases with OP, mantle material couples to the OP and resists toroidal flow deformation on the timescales of our experiments. *HLP/SRP N-S extent* red box represents the ~100 – 200 km trench-parallel (north-south) length of the HLP/SRP tracks estimated by seismic studies [e.g., *Wagner et al.*, 2012], and we've assumed a ± 50 km and ± 5 Ma error.

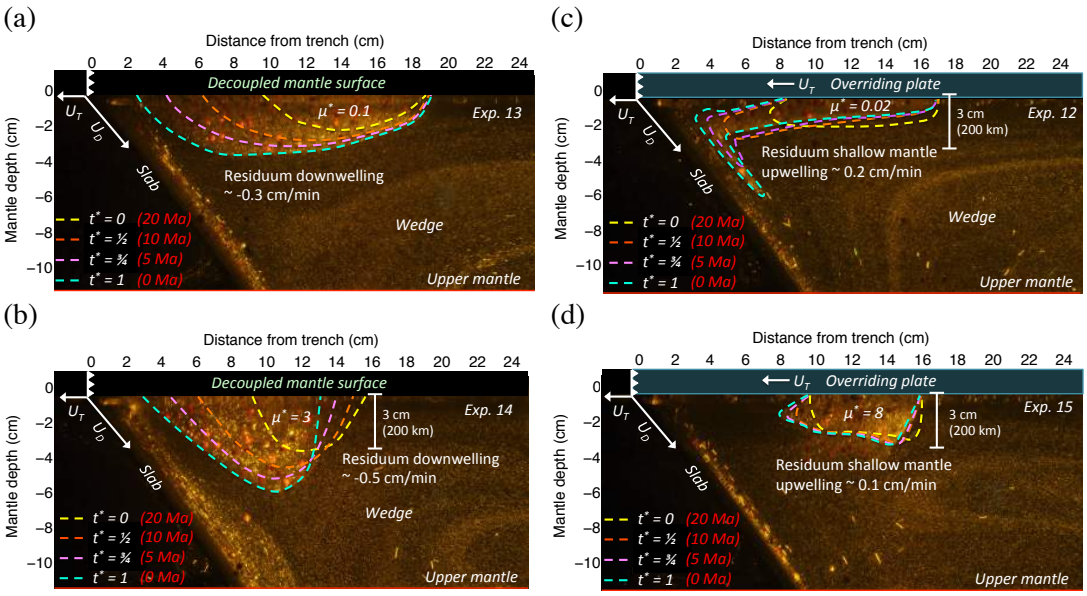

Figure 10. Comparison of 20 Ma evolution of weak and strong residuum with free slip mantle surface (a – b) and with overriding plate (c – d). Dashed lines indicate mantle-residuum interface through time. With no OP (Exp. 13 and 14), greater residuum sinking velocities (up to 0.5 cm min^{-1}) are observed in $\mu^* > 1$. With coupled mantle surface (Exp. 12 and 15), upwelling velocities are detected beneath and on the west of the residuum.

(a)

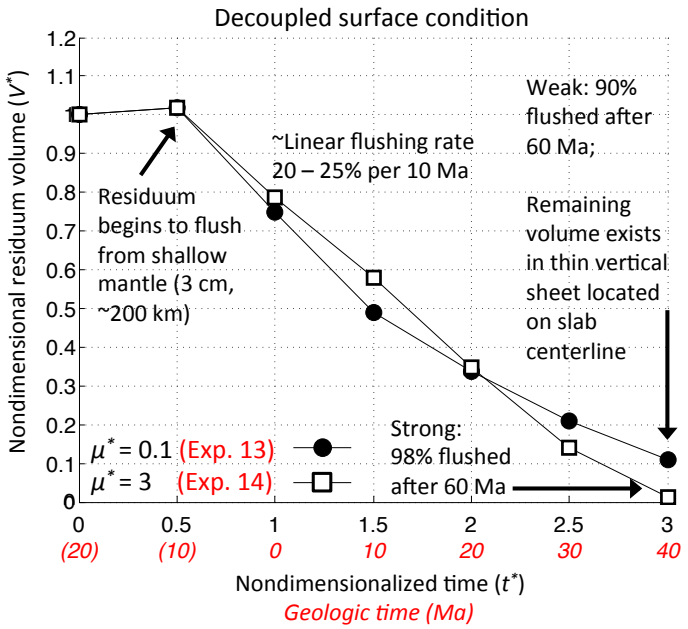

(b)

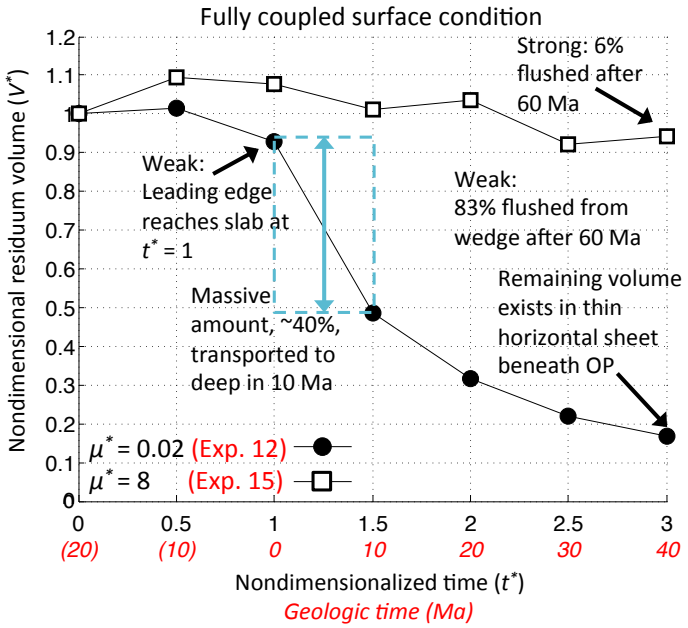

Figure 11. Shallow wedge residuum volume vs. time. Residuum volume is approximated assuming shallow mantle extends to 3 cm (~200 km) depth. Volume = side view area × residuum N-S extent (from x-y plane). Material subducted below 3 cm is considered flushed from shallow mantle. Imposing different mantle surface conditions, such as (a) free slip mantle (Exp. 13 & 14) and (b) no slip (Exp. 12 & 15), greatly changes patterns of material transport towards the trench and flushing from the shallow mantle.

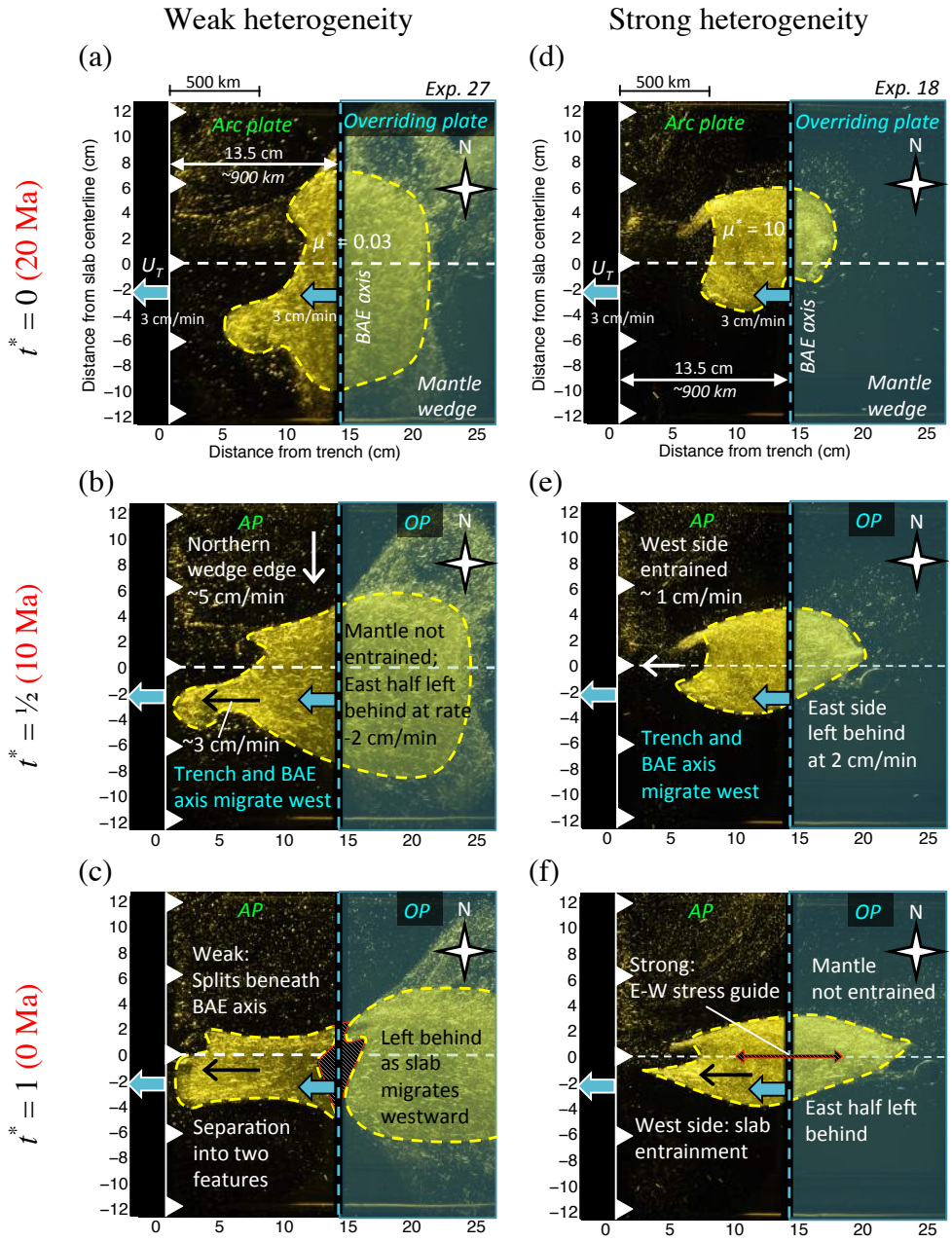

Figure 12. Low viscosity (a – c) and high viscosity (d – f) residuum beneath BAE axis with westward migration rate 3 cm min^{-1}. Rollback controlled BAE begins at $t^* = 0$. Extensional axis (green dashed line) is located ~13.5 cm (~900 km) from the trench. Residuum east of extension center is left behind as slab migrates to the west. (c) Weak heterogeneity splits into two at the extension axis. (d – f) Experiment illustrates strong stress guide effect. Viscous normal stresses limit slab-ward advection of residuum under AP. Approach velocity of western side of residuum ~1 cm min^{-1} is ~ two-thirds less than the weak heterogeneity case. After 20 Ma, this feature has remained robust throughout.

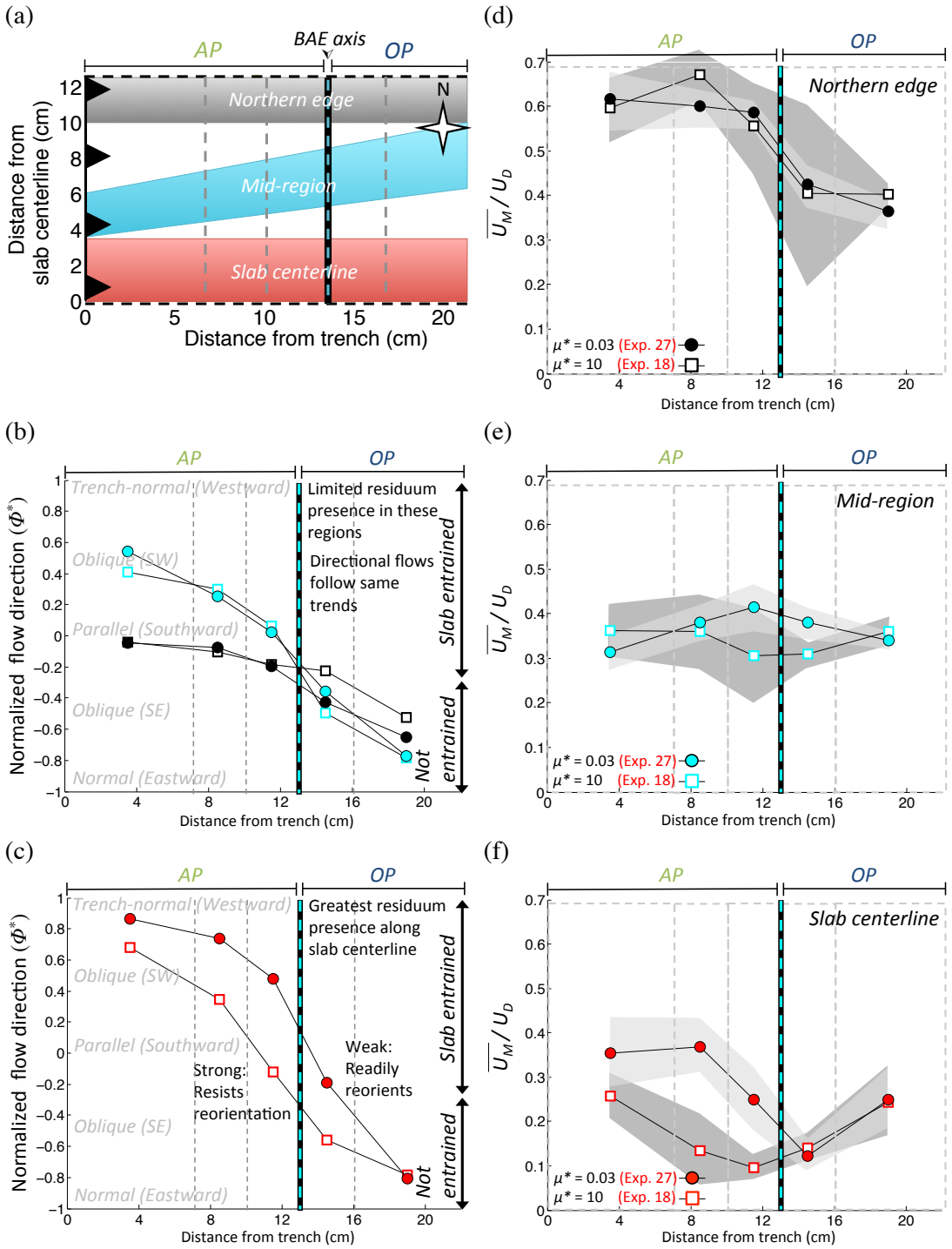

Figure 13. Normalized flow direction (Φ^*) and mean instantaneous wedge velocity (U_M/U_D) for BAE cases Exp. 27 (weak residuum) and Exp. 18 (strong residuum). The majority of the residuum mass is located in the slab centerline region and velocities in this region exhibit the greatest variation between weak and strong residuum cases.

(a)

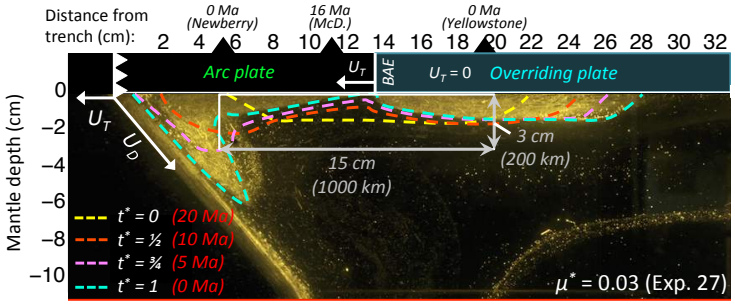

(b)

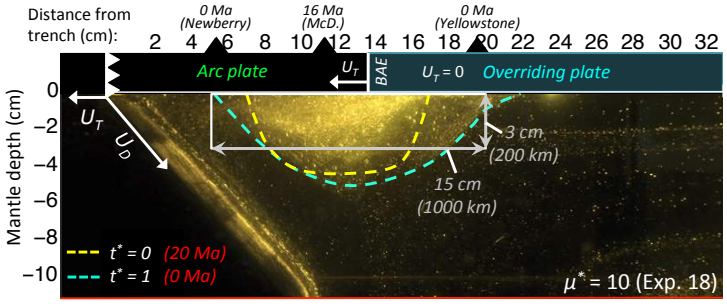

(c)

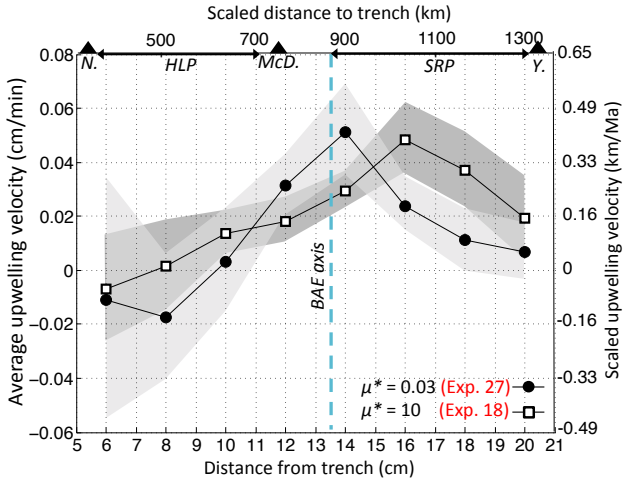

Figure 14. Side view evolution of (a) weak (Exp. 27) and (b) strong (Exp. 18) residuum located beneath a BAE axis. Dashed lines indicate residuum-wedge interface through time. For reference, approximate locations of Cascades volcanic centers Newberry (N.), McDermitt (McD.), and Yellowstone (Y.) are shown in black triangles. (c) Mean Lagrangian upwelling velocity of particles located in shallow mantle (grey box in (a) and (b)) between $t^* = 0$ and 1. Grey shading represents standard deviation about the mean.

(a)

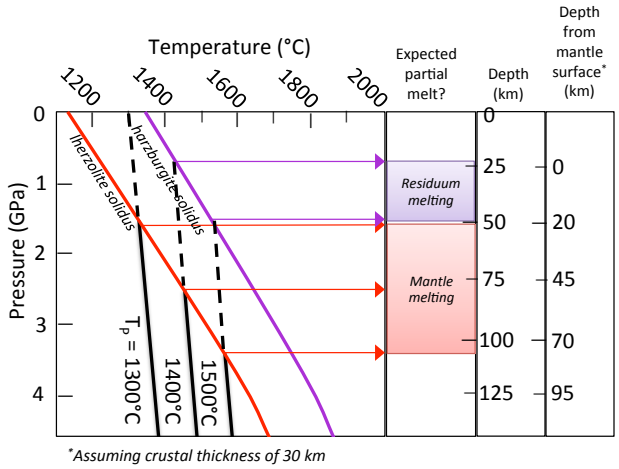

(b)

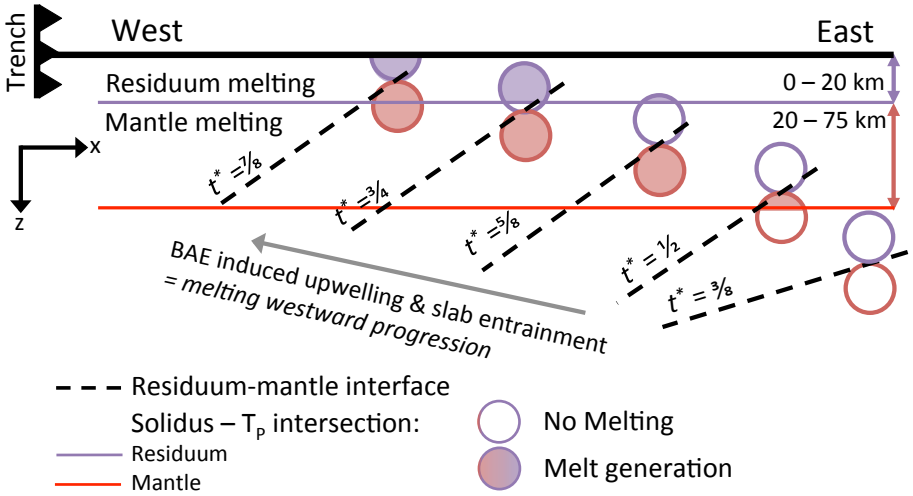

Figure 15. (a) Anhydrous P-T diagram for mantle lherzolite (red curve, from *Thompson and Gibson* [2000]), and mantle harzburgite (purple curve, from *Maaløe* [2004]). Black lines represent the adiabats for representative mantle potential temperatures (T_P). Right-hand side y-axis shows mantle depths at which decompression melting expected for lherzolite, the assumed mantle composition, and harzburgite, the assumed residuum composition. (b) Potential trajectory and timing for a low viscosity residuum interface migration beneath the HLP. Residuum evolution due to slab and BAE induced upper mantle flow fields. Trenchward shallowing of sloped residuum interface leads to westward age progressive melting beneath the HLP. Residuum evolution is a guide for melting background ambient mantle.

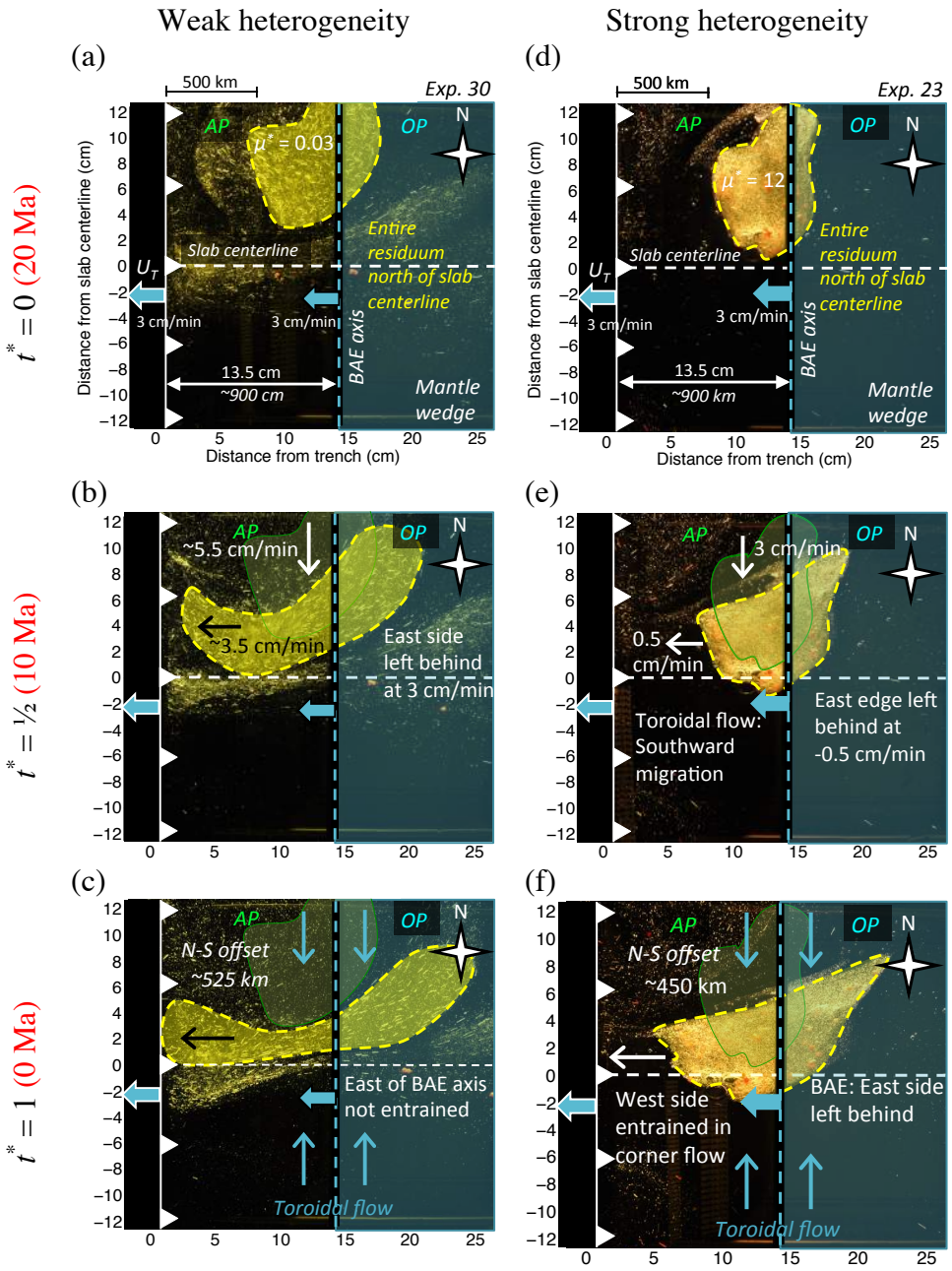

Figure 16. Time evolution of weak (a – c) and strong (d – f) residuum initially located in northern wedge beneath BAE axis with extension rate of 3 cm min^{-1}. In the $t^* = 0.5$ and $t^* = 1$ images, the initial residuum location is outlined in green for reference. Southward migration of residuum is the result of deformations induced by trench rollback.

(a)

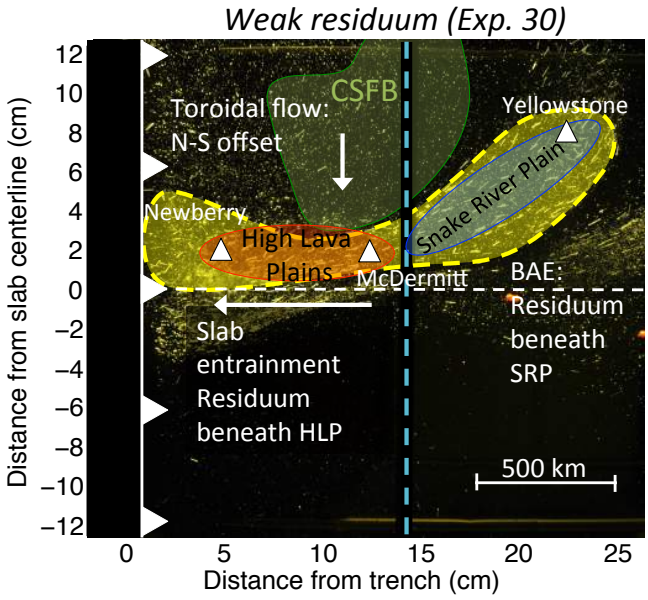

(b)

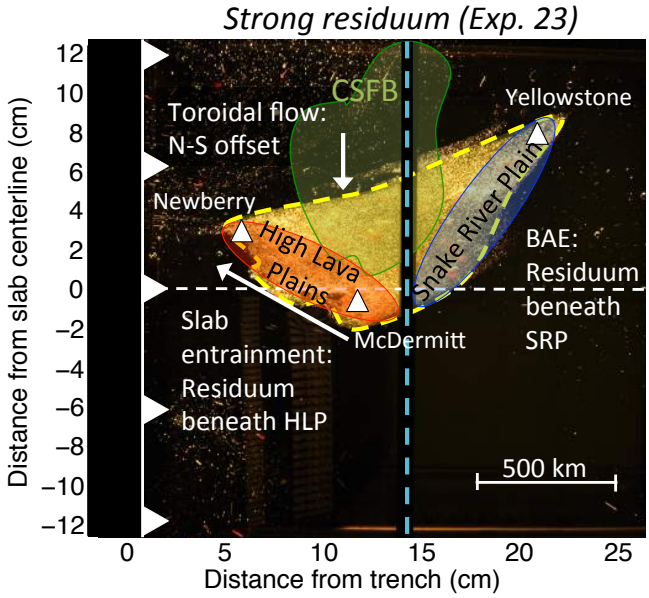

Figure 17. Annotations highlight rough estimates of key features of PNW overlaid on experiments with BAE and (a) weak (Exp. 30) and (b) strong (Exp. 23) residuum. Laboratory models represent North-south offset between the CSFB and HLP-SRP tracks are a consequence of deformations induced by trench-migration. Our experiments indicate that placement of melt residuum beneath HLP and SRP is consequence of slab and OP plate forcing allowing E-W extension of features.

SUPPLEMENTARY INFORMATION

Supplementary Figure 1. (a) Cartoon schematic illustrating set up of laboratory cameras and lightsheets used to visualize model throughout the course of the experiments. Two cameras take (b) side view and (c) map view photographs. The cameras move with the subduction apparatus at trench migration rate U_T. All photographs within the paper are in a fixed trench reference frame.

(a)

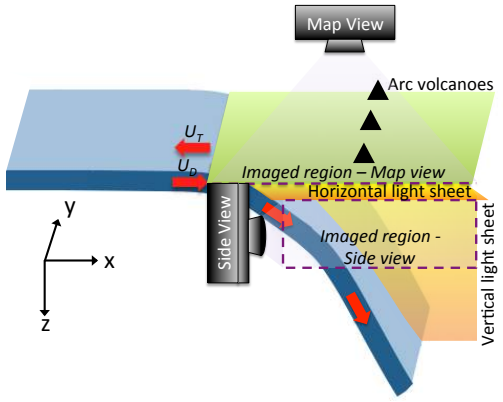

(b)

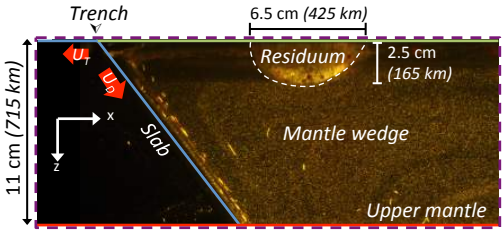

(c)

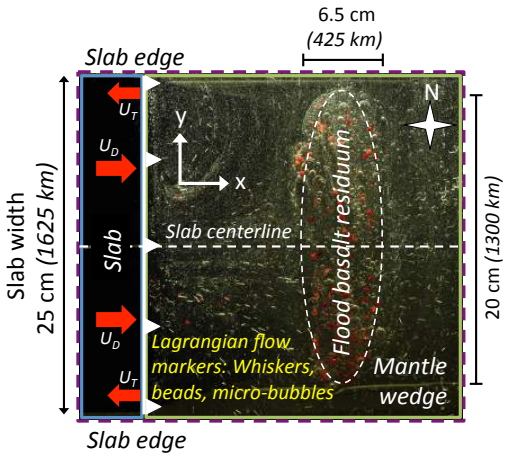

Supplementary Figure 2. All images shown in the paper are in a fixed trench reference frame. Understanding how the system moves in an absolute reference frame is important for the kinematics, seismic anisotropy, and thermochemical evolution of the upper mantle. The cartoon schematic illustrates time evolution of subduction system with back-arc extension (BAE) apparatus in an absolute reference frame. Trench and extensional axis move westward at migration rate U_T. Reference locations A, A', B, B', C, C' are shown throughout each frame to track plate motion. Mylar imposes zero horizontal surface velocity on the underlying fluid surface.

(a) $t^* = 0$ (20 Ma)

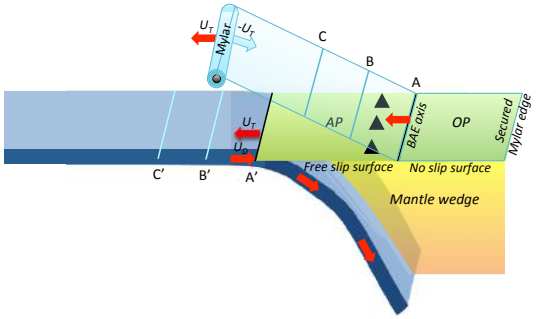

(b) $t^* = 0.5$ (10 Ma)

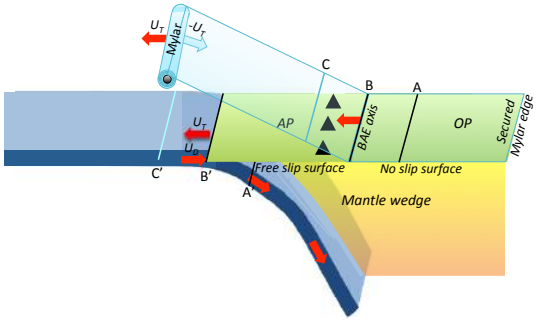

(c) $t^* = 1$ (0 Ma)

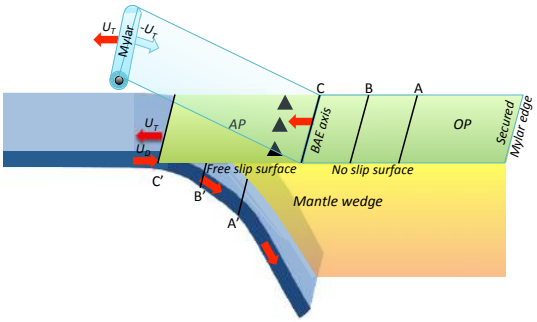

Supplementary Figure 3. Similar to Fig. 7 except velocities are calculated and displayed in an absolute reference frame. Map view wedge non-dimensional Lagrangian particle velocity (U_M/U_D) is shown at mantle depth z = 1 – 2 cm (65 – 130 km) beneath the surface for anambient mantle wedge ($\mu^* = 1$) with (a) free slip and (b) no slip mantle surface in an absolute reference frame. For each experiment location of the trench and select fluid particles are highlighted in light grey, dark grey, and black at 40 Ma, 20 Ma, and present day, respectively. With overriding plate shallow mantle velocities are dampened and oriented more strongly trenchward (westward) throughout the x-y plane due to surface-lithospheric coupling.

(a) Decoupled mantle surface

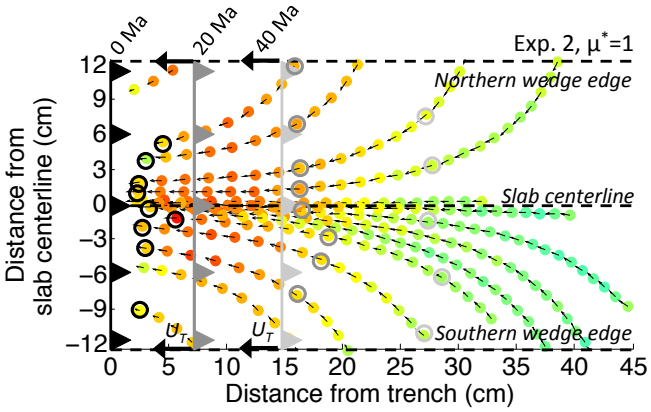

(b) Coupled mantle surface

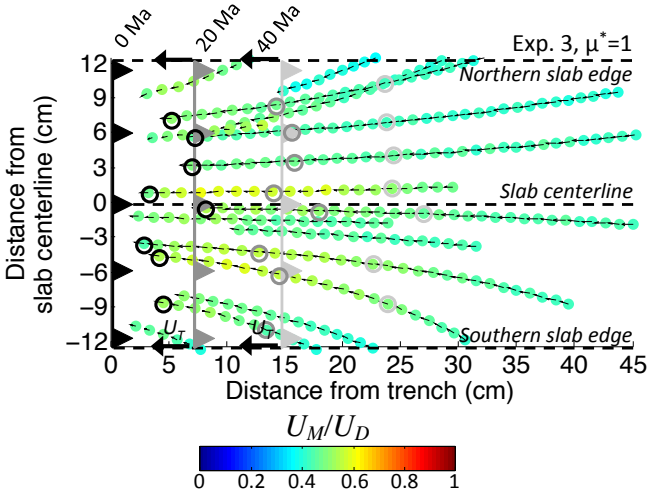

Supplementary Figure 4. The evolution of residuum in the wedge is strongly coupled to drivers of the local flow field. Varying downdip (U_D) and rollback (U_T) plate rates change the induced mantle flow with which the heterogeneity interacts. In Exp. 6 (Fig. 4a – c), the eastern residuum edge, located furthest from the trench, gets left behind in the mantle as the plate retreats and the residuum edge located closest to the slab gets entrained with the downgoing plate over the course of the experiment. Our results indicate that the relative intensity of U_T to U_D determines which wedge material will eventually be subducted in a long running system.

In a fixed trench reference frame, a mantle saddle point results in cases with migrating trench. (a) Map view, long exposure image in a fixed trench reference frame capturing ~10 Ma of evolution of mantle wedge flows (Exp. 6 shown). With respect to the trench, select relative material pathlines are shown in black and the saddle point location is highlighted with a yellow diamond. (b) Saddle point location for various slab parameters and viscosity ratios. Results indicate that the location of the saddle point is highly affected by the relative intensities of U_T and U_D, represented by the variable U^* which equals the ratio U_T / U_D. Trench migration and slab convergence rates used in the calculation of U^* for the Aleutians, Cascades, and Tonga-Kermadec subduction systems were taken from the compilation of *Long and Silver* [2009].

(a)

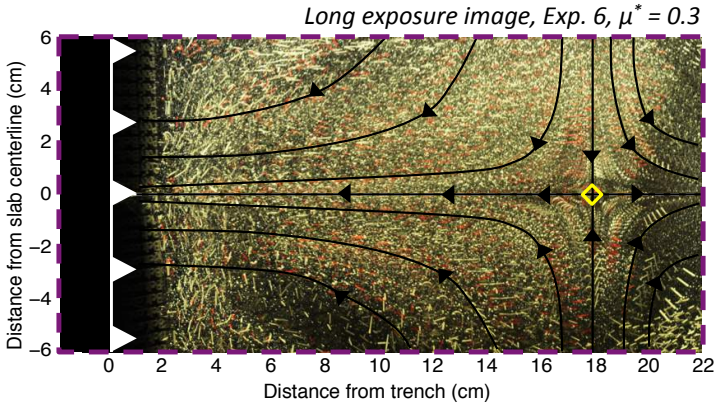
Long exposure image, Exp. 6, μ* = 0.3
Distance from slab centerline (cm)
Distance from trench (cm)

(b)

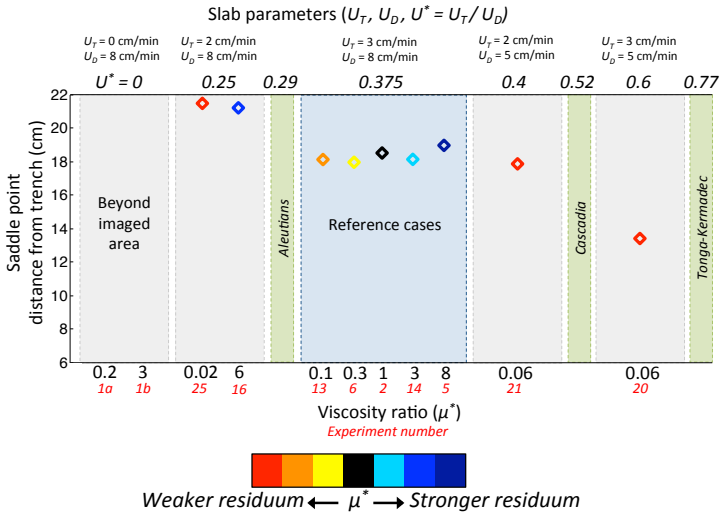
Slab parameters (U_T, U_D, U* = U_T/ U_D)
U_T = 0 cm/min
U_D = 8 cm/min
U_T = 2 cm/min
U_D = 8 cm/min
U_T = 3 cm/min
U_D = 8 cm/min
U_T = 2 cm/min
U_D = 5 cm/min
U_T = 3 cm/min
U_D = 5 cm/min
U* = 0
0.25
0.29
0.375
0.4
0.52
0.6
0.77
Saddle point distance from trench (cm)
Beyond imaged area
Aleutians
Reference cases
Cascadia
Tonga-Kermadec
0.2 3 0.02 6 0.1 0.3 1 3 8 0.06 0.06
1a 1b 25 16 13 6 2 14 5 21 20
Viscosity ratio (μ*)
Experiment number
Weaker residuum ← μ* → Stronger residuum